

USING GRAVITY
AS A PROXY FOR
STRESS ACCUMULATION
IN
COMPLEX FAULT SYSTEMS

WHICH HAS BEEN WRITTEN ON THE SPINE AS

USING GRAVITY AS A PROXY FOR
STRESS ACCUMULATION

IS WRITTEN IN ACCORDANCE WITH THE
SPECIFICATIONS FOR AN INTEGRATED-ARTICLE THESIS BY

TYLER JOSEPH HAYES

IN THE
GRADUATE PROGRAMME OF EARTH SCIENCES

A THESIS SUBMITTED IN PARTIAL FULFILMENT
OF THE REQUIREMENTS FOR
THE DEGREE OF PHILOSOPHÆ DOCTOR

FACULTY OF GRADUATE STUDIES



The UNIVERSITY of WESTERN ONTARIO

© TYLER JOSEPH HAYES
MMVII

THE UNIVERSITY OF WESTERN ONTARIO
FACULTY OF GRADUATE STUDIES

CERTIFICATE OF EXAMINATION

CHIEF ADVISOR

EXAMINING BOARD

DR. KRISTY TIAMPO

DR. CHARLES SAMMIS

ADVISORY COMMITTEE

DR. JOHN BRAUN

DR. LALU MANSINHA

DR. DAHZI JIANG

DR. HENNING RASMUSSEN

DR. SEAN SHIEH

THE THESIS BY
TYLER JOSEPH HAYES
ENTITLED
**USING GRAVITY AS A
PROXY FOR STRESS ACCUMULATION IN
COMPLEX FAULT SYSTEMS**
IS ACCEPTED IN PARTIAL FULFILMENT
OF THE REQUIREMENTS FOR THE DEGREE OF
PHILOSOPHIÆ DOCTOR

DATE

CHAIR OF EXAMINING BOARD

ABSTRACT

The gravity signal contains information regarding changes in density at all depths and can be used as a proxy for the strain accumulation in fault networks. A general method for calculating the total, dilatational, and free-air gravity for fault systems with arbitrary geometry, slip motion, and number of fault segments is presented. The technique uses a Green's function approach for a fault buried within an elastic half-space with an underlying driver plate forcing the system. A stress-evolution time-dependent earthquake fault model was used to create simulated slip histories over the San Andreas Fault network in California. Using a linear sum of the gravity signals from each fault segment in the model, via coseismic gravity Green's functions, a time-dependent gravity model was created. The steady-state gravity from the long term plate motion generates a signal over five years with magnitudes of $\pm \sim 2 \mu\text{Gal}$; the current limit of portable instrument observations. Moderate to large events generate signal magnitudes in the range of $\sim 10 \mu\text{Gal}$ to $\sim 80 \mu\text{Gal}$, well within the range of ground based observations. The complex fault network geometry of California significantly affects the spatial extent of the gravity signal from the three events studied. Statistical analysis of 55 000 years of simulated slip histories were used to investigate the use of the dilatational gravity signal as a proxy for precursory stress and strain changes. Results indicate that the precursory dilatational gravity signal is dependent upon the fault orientation with respect the tectonic loading plate velocity. This effect is interpreted as a consequence of preferential amplification of the shear stress or reduction of the nor-

mal stress, depending on the steady-state regime investigated. Finally, solutions for the corresponding gravity gradients of the coseismic dilatational gravity signals are developed for a vertical strike-slip fault. Gravity gradient solutions exhibit similar spatial distributions as those calculated for Coulomb stress changes, reflecting their physical relationship to the stress changes. The magnitude of the signals, on the order of $1 \times 10^{-4} E$, are beyond the resolution of typical exploration instruments at the present time.

KEYWORDS: NUMERICAL SOLUTIONS; SEISMIC CYCLE; GRAVITY; GRAVITY GRADIENTS; TIME VARIABLE GRAVITY; EARTHQUAKE INTERACTION, FORECASTING, AND PREDICTION.

Co-AUTHORSHIP

Research for the project was done by Tyler Joseph Hayes. Dr. Tiampo provided funding at various stages throughout the research and revised all chapters. Dr. Rundle made available the Virtual California code for my use to incorporate into the project. Both, Dr. Rundle and Dr. Fernández, provided suggestions for Chapter 1, Chapter 2, and Chapter 4.

PIGRAPH

And the blindness of the blind man and his seeking and groping shall yet bear witness to the power of the sun into which he gazed—did you know that before?

And the enlightened man shall learn to build with mountains! It is a small thing for the spirit to move mountains—did you know that before?

You know only the sparks of the spirit: but you do not see the anvil which the spirit is, nor the cruelty of its hammer!

THUS SPOKE ZARATHUSTRA

— *Friedrich Nietzsche*



DEDICATION

For Mom and Dad.

ACKNOWLEDGEMENTS

People who matter are most aware
that everyone else does, too.

Malcolm Forbes

Throughout the course of the past several years, there have been those without whom this project would never have been completed. My supervisor, Kristy Tiampo, has constantly supported my efforts to explore various aspects of the role gravity might play in helping to identify stress and strain accumulation. Sometimes these diversions even proved fruitful! Kristy always encouraged me to attend conferences and develop working relationships beyond the halls of Western. For all of her support, for all of her guidance, for her taking a chance on a student she met briefly over breakfast, I sincerely wish to thank Kristy for the opportunity to work on this project.

Of course, to go without mentioning Lalu Mansinha and Henning Rasmussen would be just short of a sin. Lalu always made himself available for panicked discussions on various aspects of deformation theory, coordinate systems, and the like. This is including coming in to meet me on Good Friday one year (which became the “Good Friday” version of `GRAV_GREEN.f90`). Lalu’s laughter calming a stressed student will be missed. Henning was always available (when not in Korea!) to discuss various aspects of computational methods, for course or thesis work, and encouraged me to enter into the Graduate Programme of Scientific Computing. I’m glad I took his advice, and I’m glad to have worked with him on this project.

John Rundle and José Fernández proved to be as supportive of my project as my supervisor's were. The work on Virtual California would not have taken place without his help, period. But his efforts did not end there. John was always free to answer any queries I would e-mail him, and discussions with him on the physics of the models, or new ideas of mine, always led to further insight. José (whom I have the pleasure of calling Pepe), has always encouraged me to explore my work on gravity and, in particular, was ever diligent in perusing the gravity gradient work. His suggestions to improve the arguments always led to more discoveries and further understanding on my part. For both of their support of a student who was not their charge, I sincerely thank them.

Have you ever banged your head against a wall in order to get a computer set up, to get it working correctly, or trying to install some esoteric, academic specific piece of software/junk? I haven't. I was fortunate enough to have John Brunet, Barry Price, and the in-house Linux guru, Bernie Dunn, to make sure I never had those problems. Their tireless efforts behind the scenes made sure I was able to focus on the research at hand. Indeed, they provided me with the tools necessary to pull this thesis together.

In general, it can be said that Friday's are good for two reasons. The first is that it's the end of the week. The second reason, until now, has only been known to those of us fortunate enough to walk the hallways of B&G, and it is this: Mary Rice always had homemade snacks and goodies in her office. Mary's help extended beyond the Friday treats. Mary always make sure that all of the small details were taken care of, and when the weren't she helped fix them, even it was a loose end on a wool sweater.

I would hate to forget listing any of my friends who helped make this thesis possible, so instead, I'll thank you all at once. To the Usual

Gang of Idiots, you know who you are, thanks for being there.

Last, but by no means least, my family has always been supportive of me throughout my thesis and without them I'm not sure where I would be. Words escape me. Thank you.

CONTENTS

TITLE PAGE	i
CERTIFICATE OF EXAMINATION	ii
ABSTRACT	iii
Co-AUTHORSHIP	v
EPIGRAPH	vi
DEDICATION	vii
ACKNOWLEDGEMENTS	viii
CONTENTS	xi
LIST OF FIGURES	xv
LIST OF APPENDICES	xvii
INTRODUCTION	I
CHAPTER I	
CALCULATING CO-SEISMIC GRAVITY CHANGES	9
I.1 INTRODUCTION	9
I.2 THEORY	II
I.2.1 GRAVITY GREEN'S FUNCTIONS	II
I.2.2 EXTENSION TO A COMPLEX FAULT NETWORK . . .	14

I.3	IMPLEMENTATION	17
I.3.1	CODE OVERVIEW	17
I.3.2	GRAV_GREEN.F90	19
I.3.3	GRAVITY.F90	22
I.3.4	GRAVITY90_VIEW.PRO	24
I.4	EXAMPLES	25
I.4.1	JOSHUA TREE-LANDERS-HECTOR MINE	25
I.4.2	THE ALASKA GOOD FRIDAY EARTHQUAKE, 1964	26
I.5	DISCUSSION AND CONCLUSION	30
	REFERENCES	31

CHAPTER 2

	GRAVITY CHANGES FOR CALIFORNIA	34
2.1	INTRODUCTION	34
2.2	EVOLUTIONARY EARTHQUAKE MODELS	38
2.3	VIRTUAL CALIFORNIA	39
2.3.1	THE SIMULATION ALGORITHM	40
2.4	GRAVITY GREEN'S FUNCTIONS	44
2.4.1	POTENTIAL CHANGES	45
2.4.2	GRAVITY FOR A FINITE FAULT	46
2.5	VIRTUAL GRAVITY	49
2.5.1	GRAVITY CALCULATIONS	49
2.5.2	GREEN'S FUNCTIONS	50
2.6	RESULTS	54
2.6.1	STEADY-STATE GRAVITY	54
2.6.2	LARGE EVENT GRAVITY SIGNALS	55
2.6.3	MODERATE SIZE EXAMPLE	59
2.7	CONCLUSIONS	61
	REFERENCES	66

CHAPTER 3

GRAVITY IN EARTHQUAKE NUCLEATION	71
3.1 INTRODUCTION	71
3.2 METHOD	72
3.2.1 GENERATING THE SLIP HISTORIES	73
3.2.2 GRAVITY CALCULATIONS	74
3.2.3 FILTERING THE STEADY-STATE TREND	74
3.2.4 THE GRAVITY STATISTICS	75
3.3 RESULTS	76
3.4 DISCUSSION	77
REFERENCES	84

CHAPTER 4

GRAVITY GRADIENTS OF DEFORMATION FIELDS	87
4.1 INTRODUCTION	87
4.2 THE GRAVITY GRADIENT SOLUTIONS	88
4.3 RESULTS	91
4.4 DISCUSSION	97
REFERENCES	98

CONCLUSIONS	102
-------------	-----

APPENDICES	106
------------	-----

CIRICULUM VITA	109
----------------	-----

LIST OF FIGURES

1.1	COORDINATE SYSTEM USED	13
1.2	GRAVITY CODE FLOW DIAGRAM	18
1.3	JOSHUA TREE SEQUENCE EXAMPLE	27
1.4	GOOD FRIDAY, ALASKA 1964, EARTHQUAKE	29
2.1	FAULT MODEL	41
2.2	COORDINATE SYSTEM	47
2.3	STEADY-STATE TOTAL GRAVITY	55
2.4	STEADY-STATE DILATATIONAL GRAVITY	56
2.5	STEADY-STATE FREE-AIR GRAVITY	57
2.6	SAN FRANCISCO 1906 EXAMPLE	58
2.7	FORT TEJON EXAMPLE	60
2.8	MODELLED SLIP FOR AN EVENT AT BRAWLEY.	61
2.9	FIVE YEARS DILATATIONAL GRAVITY FOR BRAWLEY	62
2.10	TEN YEARS DILATATIONAL GRAVITY FOR BRAWLEY	63
2.11	TEN YEARS TOTAL GRAVITY FOR BRAWLEY	64
2.12	GRAVITY FOR THE BRAWLEY EVENT	65
3.1	FAULT MAP OF VIRTUAL CALIFORNIA	77
3.2	PLOT OF $P_i^{\Delta g}$ FOR THE SAF AND NORTHERN SAF	78
3.3	PLOT OF $P_i^{\Delta g}$ FOR THE BIG BEND AND MOJAVE FAULTS	79
3.4	MAP PLOT OF $P_i^{\Delta g}$ FOR THE BIG BEND	80
3.5	MAP PLOT OF $P_i^{\Delta g}$ FOR THE NORTHERN SA	81
4.1	VERTICAL GRAVITY GRADIENT	91
4.2	HORIZONTAL GRAVITY GRADIENTS	93

4.3	COMBINED GRADIENTS WITH DIFFERENT ϵ VALUES	94
4.4	GRAVITY GRADIENT SOLUTION FOR JOSHUA TREE	95
4.5	JOUSHUA TREE COULOOOMB STRESS CHANGES	96
B.I	FACSIMILE OF THE COPYRIGHT RELEASE FOR CHAPTER 2	108

LIST OF APPENDICES

A	CODE LISTINGS	106
B	COPYRIGHT PERMISSIONS	107
B.1	COAT OF ARMS	107
B.2	JOURNAL OF GEOPHYSICAL RESEARCH	108

INTRODUCTION

The discovery of truth is prevented more effectively, not by the false appearance things present and which mislead into error, not directly by weakness of the reasoning powers, but by preconceived opinion, by prejudice.

Arthur Schopenhauer



PREDICTING earthquakes has long been a goal of earth scientists in order to mitigate the social, economic, and environmental impacts of their effects. However, due to the complexity of the physical processes that drive the tectonic plates, a fully deterministic approach is not yet feasible. Despite the inherent difficulties, researchers are now able to more accurately describe the subsurface strains and stresses acting on active faults. Current methods for estimating subsurface stress and strain employ a wide range of tools: GPS (*Williams et al., 2006*), InSAR (*Massonnet et al., 1993*), combined GPS and InSAR (*Samsonov and Tiampo, 2006*), and measurements of strain at the surface (*Hagiwara, 1974*). Other methods include statistical analysis of seismicity patterns (*Tiampo et al., 2002; Bowman and King, 2001*), and theoretical calculations of the post-seismic change in the Coulomb stress (*King et al., 1994; Deng and Sykes, 1997*). Seismic triggering appears to play a significant role in identifying regions of increased seismic risk (*Freed, 2005*), and more recent studies by *Chen*

et al. (2006) suggest that even on very short time scales, seismic triggering occurs on the rupture front itself via similar mechanisms that govern regional processes.

Investigations into patterns of seismicity, developed in recent years, present promising methods by which researchers can identify regions of seismic risk. Their basis relies not on the solution of a deterministic expression governing the seismic process (likely non-linear and as of yet, unknown (*Rundle et al.*, 2004)), but rather a statistical analysis of the space-time surface expression of those dynamics, i.e., seismicity. Observations of accelerating moment release (*Bowman and King*, 2001; *Mignan et al.*, 2006), and pattern informatics (*Tiampo et al.*, 2002; *Holliday et al.*, 2006) offer researchers accurate methods for the identification of small perturbations to the long-term, background seismicity rates. These perturbations can then be used to identify regions of increased seismic risk.

In other methods, such as Coulomb stress triggering (*King et al.*, 1994; *Deng and Sykes*, 1997), the physical parameters used to constrain models of the subsurface stress and strain are inherently unobservable by in-situ observations. Stress and strain values at depth must be inferred by their expression at the surface. Direct observation of Coulomb stress changes are not possible as the quantity must be calculated and interpreted, never measured. The problem of estimating subsurface stress and strain is further compounded by the difficulties posed by using surface measurements of strain. Research by *Tullis* (1996) suggests that instruments located at the surface lack the resolution to properly quantify the subsurface stresses on time scales required for prediction. Although, *Tullis* (1996) does acknowledge that long-term monitoring techniques may identify regions of relative increases and, by extension, seismic risk.

Improvements of observational techniques of surface deformation

in the past decade are now capable of resolving changes with high temporal resolution (e.g., GPS), and over large spatial scales (e.g., InSAR). Combining these complementary data sets, as first demonstrated by *Samsonov and Tiampo* (2006), can further constrain their independent estimates of deformation. Seismicity itself, the product of the released subsurface stress and strain, can act as proxy for stress, as demonstrated by *Dieterich et al.* (2000), whom successfully used seismicity to model the stress changes at the Kilauea volcano.

Nonetheless, such measurements are still limited to measuring the surface expression of the underlying physical parameters. Gravity, by comparison, contains information from all depths and its solution is rendered unique by imposing a known fault geometry (*Skeels*, 1947). As such, the use of gravity data may offer researchers a viable method to further constrain subsurface strain and stress resulting from the redistribution of mass following seismic activity.

Using gravity in seismically active regions is not a new concept. Previous studies of gravity measurements, correlating both strain and elevation changes, led researchers to suggest the creation a gravity monitoring network for California (*Jachens et al.*, 1983), and absolute gravimeters have recorded observable gravity changes following an earthquake (*Tanaka et al.*, 2001). Furthermore, studies of trench parallel gravity anomalies (TPGA) demonstrate strong correlation of the residual free-air gravity anomaly with hypocentral locations (*Song and Simons*, 2003). In subduction zone systems, the magnitudes of the free-air gravity anomalies are well within observational limits. However, the use of gravity in systems with strike-slip faults is not routinely practised, as the magnitudes of the dilatational component of gravity, corresponding to subsurface density changes from seismic redistribution of matter, are orders of magnitude smaller than in subduction zones. Nonetheless, recent improvements to portable instruments now allow

consistent measurements on the order of μGal , and permanent superconducting gravimeters (SGs), are able to resolve nGal signals. In light of these new instrumentation advances, gravity may offer researchers a viable method to complement the traditional suite of observational tools used to estimate subsurface stress and strain. Through computer simulations, this thesis intends to examine the potential uses gravity may offer researchers to constrain these parameters, as well as what new insights into the underlying physics of earthquakes gravity may offer.

Through the use of computer models, we are able to investigate simulated slip-histories over thousands of years and examine long-term patterns that may develop in the system. Allowing us to investigate whether regions exhibit certain behaviour based on geometry with respect to other faults, or communicate stress via a highly complex system such as a neural network. By incorporating the gravity solutions into the computer models, we can begin to examine what role gravity may play in the theatre of earthquake dynamics, and potentially the forecasting of its temporal evolution. Gravity provides an intuitive interpretation by which one can understand the underlying physics that drives the fault system. This would enable earthquake forecasters to constrain their methods with additional information, *viz*, gravity.

This thesis seeks not to be a lengthy mathematical treatise on the relationship between gravity, stress, and strain, but rather an investigation into the practical application of using gravity as a proxy for subsurface stress and strain accumulation. Indeed, the physical relationship between gravity and stress was clearly established almost three decades ago by *Walsh and Rice (1979)*. As this thesis will demonstrate, gravity does indeed provide important information on the spatial and temporal evolution of the constitutive processes of earthquake gener-

ation and holds significant promise as tool for seismic hazard mitigation. To investigate the practical application of gravity as a proxy for stress and strain accumulation, the thesis is organized as follows.

In Chapter 1, accepted for publication in *Computers & Geosciences*, the single-plane solutions of gravity changes are adapted for complex fault networks fault segments that have arbitrary orientation, dip, and slip-mechanisms in an elastic half-space. FORTRAN90 codes and example data sets are provided as an appendix in electronic format to allow researchers to apply the method in their own investigations, and an IDL visualization routine is provided to facilitate visualization.

In Chapter 2, we apply the method outlined in Chapter 1 to California using the Virtual California (VC) stress-evolution model as published in Hayes *et al.* (2006). The steady-state gravity signal is discussed, and an examination of several sequences is presented. Results indicate that both the steady-state and co-seismic gravity signals are heavily influenced by the geometry of the fault network.

In Chapter 3, submitted to *Geophysical Research Letters*, a more thorough analysis of gravity as a potential proxy for stress accumulation is undertaken. Using 55 000 years of slip histories generated by VC, we investigate the triggering of earthquakes by unstable seismic slip and investigate how the dilatational gravity signal identifies this phenomenon. Orientation of the fault segments with respect to the plate velocities appear to contribute in significant manner to the type of signal observed and the associated nucleation mechanism.

In Chapter 4, the solutions for the gravity gradients for a single, vertical, strike-slip fault in an elastic half-space are presented (submitted to *Geophysical Journal International*). The gravity gradient's connection to the observed spatial distribution of the subsurface deformation field is discussed in context with its relationship to the changes in Coulomb stress changes. The spatial correlations between the calcu-

lated Coulomb stress changes and the modelled gravity gradients are compelling.

Finally, in the Conclusion section, the findings of this thesis are summarized and suggestions for further research are presented.

REFERENCES

- Bowman, D. D., and G. C. P. King, Accelerating seismicity and stress accumulation before large earthquakes, *Geophys. Res. Lett.*, 28, 4039–4042, 2001.
- Chen, Y., C. G. Sammis, and T. Teng, A high-frequency view of the 1999 Chi-Chi, Taiwan, source rupture and fault mechanics, *Bull. Seis. Soc. Amer.*, 96(3), 807–820, doi:10.1785/0120050059, 2006.
- Deng, J., and L. R. Sykes, Stress evolution in southern California and triggering of moderate-, small-, and micro-size earthquakes, *J. Geophys. Res.*, 102(B11), 24,411–24,435, 1997.
- Dieterich, J., V. Cayol, and P. Okubo, The use of earthquake rate changes as a stress meter at Kilauea volcano, *Nature*, 408, 457–460, 2000.
- Freed, A. M., Earthquake triggering by static, dynamic, and postseismic stress transfer, *Annu. Rev. Earth. Planet. Sci.*, 33, 335–367, doi:10.1146/annurev.earth.33.092203.122505, 2005.
- Hagiwara, Y., Probability of earthquake occurrence as obtained from a Weibull analysis of crustal strain, *Tectonophysics*, 23, 313–318, 1974.
- Hayes, T. J., K. F. Tiampo, J. B. Rundle, and J. Fernández, Gravity changes from a stress evolution earthquake simulation of California, *J. Geophys. Res.*, 111, B09,408, doi:10.1029/2005JB004092, 2006.

- Holliday, J. R., J. B. Rundle, K. F. Tiampo, W. Klein, and A. Donnellan., Modification of the pattern informatics method for forecasting large earthquake events using complex eigenvectors, *Tectonophysics*, 413, 87–91, 2006.
- Jachens, R. C., W. Thatcher, C. W. Roberts, and R. S. Stein, Correlation of changes in gravity, elevation, and strain and southern California, *Science*, 219, 1215–1217, 1983.
- King, G. C. P., R. S. Stein, and J. Lin, Static stress changes and the triggering of earthquakes, *Bull. Seis. Soc. Amer.*, 84(3), 935–953, 1994.
- Massonnet, D., M. Rossi, C. Carmona, F. Adragna, G. Peltzer, K. Feigl, and T. Rabaute, The displacement field of the Landers earthquake mapped by radar interferometry, *Nature*, 364(6433), 138–142, doi:10.1038/364138a0, 1993.
- Mignan, A., D. D. Bowman, and G. C. P. King, An observational test of the origin of accelerating moment release before large earthquakes, *J. Geophys. Res.*, 111, B11,304, doi:10.1029/2006JB004374, 2006.
- Rundle, J. B., P. B. Rundle, A. Donnellan, and G. Fox, Gutenberg-Richter statistics in topologically realistic system-level earthquake stress-evolution simulations, *Earth Planets Space*, 56, 761–771, 2004.
- Samsonov, S., and K. Tiampo, Analytical optimization of a DInSAR and GPS dataset for derivation of three-dimensional surface motion, *IEEE Geoscience and Remote Sensing Letters*, 3(1), 107–111, 2006.
- Skeels, D. C., Ambiguity in gravity interpretation, *Geophysics*, 12, 43–56, 1947.

- Song, T.-R. A., and M. Simons, Large trench-parallel gravity variations predict seismogenic behavior in subduction zones, *Science*, 301, 630–633, 2003.
- Tanaka, Y., S. Okubo, M. Machida, I. Kimura, and T. Kosuge, First detection of absolute gravity changes caused by earthquake, *Geophys. Res. Lett.*, 28(15), 2979–2981, 2001.
- Tiampo, K. F., J. B. Rundle, S. A. McGinnis, and W. Klein, Pattern dynamics and forecast methods in seismically active regions, *Pure Appl. Geophys.*, 159(10), 2429–2467, 2002.
- Tullis, T. E., Rock friction and its implications for earthquake prediction examined via models of Parkfield earthquakes, *Proc. Natl. Acad. Sci. USA*, 93, 3803–3810, colloquim paper, 1996.
- Walsh, J. B., and J. R. Rice, Local gravity changes resulting from deformation, *J. Geophys. Res.*, 84(B1), 165–170, 1979.
- Williams, T. B., H. M. Kelsey, and J. T. Freymueller, Gps-derived strain in northwestern California: Termination of the San Andreas fault system and convergence of the Sierra NevadaGreat Valley block contribute to southern Cascadia forearc contraction, *Tectonophysics*, 413, 171–184, doi:10.1016/j.tecto.2005.10.047, 2006.

CHAPTER I

A GENERAL METHOD FOR CALCULATING CO-SEISMIC GRAVITY CHANGES IN COMPLEX FAULT SYSTEMS

A proof is a proof. What kind of a proof? It's a proof. A proof is a proof. And when you have a good proof, it's because it's proven.

*Jean Chrétien
(Former Prime Minister of Canada)*

1.1 INTRODUCTION



URRENTLY, the standard methods employed for determining the distribution of local and long-range effects from earthquakes have focused on altered topography, stress and strain, and Coulomb stress field changes realized within the system (*Chinnery, 1963; Rundle and Jackson, 1977; Okada, 1992; King et al., 1994*). It has been suggested that mapping the gravity field distribution may also act as a proxy for the stress and strain accumulation at depth in a geometrically complex fault system (*Okubo, 1992; Hayes et al., 2006*). Gravity has the advantage that it is directly measurable and further, its measurement contains information from all depths, whereas strain

[‡]A version of this chapter has been accepted for publication in Computers & Geosciences, and is pre-printed here by their permission.

meters are limited to *in situ* measurements (and subsequent approximations for strain at depth) and the Coulomb stress field is inherently non-measurable. As such, the gravity field offers additional information which can be used in conjunction with traditional methods to further identify regions of potential seismic risk.

Okubo (1992) developed the gravity Green's functions for a fault with arbitrary dip within an elastic half-space. However, the solutions of *Okubo* (1992) are only for a single fault orientation within the medium. More recently, *Soldati et al.* (1998) developed the expressions for a visco-elastic medium but, once again, the solutions are valid only for a single fault. Including arbitrary fault orientations with many faults allows one to calculate the gravity field for more realistic systems such as southern California. By including the complex fault system geometries, one can more accurately describe the resultant stress and strain (*Li and Liu*, 2006) and gravity fields (*Hayes et al.*, 2006) in the system. Moreover, the magnitude of visco-elastic effects may be mitigated by accounting for realistic fault geometries.

In this paper, we present a method for calculating the gravity field for fault systems with complex geometry and arbitrary slip motion driven by an underlying plate to allow the system to accumulate a steady-state component during periods of quiescence. The accompanying routines are simple to use and can be run on a desktop system with a Fortran90 compiler. The method is a useful tool for researchers, applicable to problems of gravity accumulation in fault systems and for evaluating the expected gravity signal in Trench Parallel Gravity Anomalies (TPGA) studies. The visualization routine facilitates interactive analysis of the resultant gravity field and increased productivity. For those with access to IDL, a visualization routine is provided or it can be used as pseudo-code for MATLAB, GMT, SciPy with Matplotlib, or R users.

In Section 1.2, we present the underlying mathematical framework employed in the routines, focusing on the extensions made to the Green's functions of *Okubo* (1992). We account for arbitrary fault segments and geometry, as well as the inclusion of an underlying driver-plate in the system, allowing for the steady-state gravity field calculation. Section 1.3 describes the practical aspects of implementation of the Green's function calculations and the interactive time-differencing scheme used in the calculating the gravity changes. The visualization routine and some examples are also presented in Section 1.3, followed by their discussion in Section 1.4. Concluding remarks on the method are provided in Section 1.5.

1.2 THEORY

1.2.1 GRAVITY GREEN'S FUNCTIONS

The calculation of the gravity field for a complex fault system, with arbitrary dip, slip, number segments, makes use of the solutions of *Okubo* (1992) for a finite fault. As our intention is not to reproduce the results of *Okubo* (1992), the final results are simply quoted here for convenience. For a complete derivation of those solutions, the reader is referred to that article. We outline here how the Green's functions of are extended to include multiple segments as well as an underlying driving plate that incorporates a steady-state component into the system in order to determine how the gravity signal develops over time.

Using the coordinate system in Figure 1.1, *Okubo* (1992) obtains for the coseismic change in gravity, Δg , of a finite fault plane evaluated

at the surface, i.e., $x_3 = 0$, a solution of the form,

$$\Delta g(x_1, x_2, x_3 = 0) = \left\{ \rho G \left[U_1 S_g(x_1, x_2; \xi, \eta) + U_2 D_g(x_1, x_2; \xi, \eta) \right. \right. \\ \left. \left. + U_3 T_g(x_1, x_2; \xi, \eta) \right] + \Delta \rho G U_3 C_g(x_1, x_2; \xi, \eta) \right\} || - \beta \Delta h(x_1, x_2) \quad (1.1)$$

Where we have used the double vertical notation of *Chinnery* (1961). The free-air gravity gradient is given by $\beta = 0.309e^{-5} \text{m/s}^2$, $\Delta \rho$ is the difference in density between the cavity filling matter and the original medium, i.e., $\Delta \rho = \rho' - \rho$. The functions, $S_g(x_1, x_2; \xi, \eta)$, $D_g(x_1, x_2; \xi, \eta)$, $C_g(x_1, x_2; \xi, \eta)$, and $T_g(x_1, x_2; \xi, \eta)$ are gravity Green's function contributions from the strike-slip, dip-slip, cavity filling, and tensile components respectively. We further note that (ξ, η) is source point on the finite fault and (x_1, x_2) is the observation point on the surface.

The function $\Delta h(x)$ in (1.1), evaluated at $x = (x_1, x_2, x_3 = 0)$, records the elevation change and is given by *Okada* (1985) as,

$$\Delta h(x) = \frac{1}{2\pi} \left[U_1 S_h(x_1, x_2; \xi, \eta) + U_2 D_h(x_1, x_2; \xi, \eta) \right. \\ \left. + U_3 T_h(x_1, x_2; \xi, \eta) \right] || \quad (1.2)$$

Where the subscript h indicates the Green's function for height change. For the gravity change free from the effect of the vertical displacement of the ground, $\Delta h(x_1, x_2)$, *Okubo* (1992) provides the following expression,

$$\Delta g^*(x_1, x_2) = \left\{ \rho G \left[U_1 S_g^*(x_1, x_2; \xi, \eta) + U_2 D_g^*(x_1, x_2; \xi, \eta) \right. \right. \\ \left. \left. + U_3 T_g^*(x_1, x_2; \xi, \eta) \right] + \Delta \rho G U_3 C_g(x_1, x_2; \xi, \eta) \right\} || \quad (1.3)$$

For our study, we currently do not calculate the cavity filling matter component in the routine, i.e, we assume $\Delta \rho = 0$. We further note

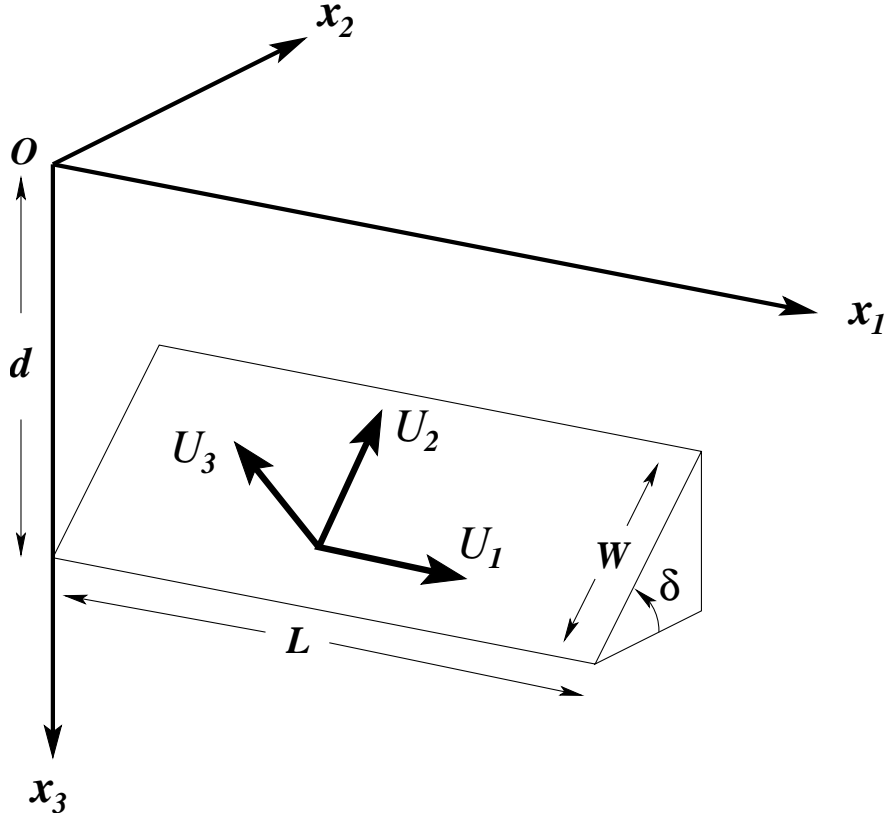


FIGURE I.I: The coordinate system with origin O , and the source model geometry used for the calculation of the gravity Green's functions. See text for symbol meanings. The footwall is shown, and the arrows indicate motion of the hanging wall. Modified after *Okubo* (1992).

that the notation $x = (x_1, x_2)$ will imply $x = (x_1, x_2, x_3 = 0)$, and similarly, $X_g(\xi, \eta)$ will imply $X_g(x_1, x_2; \xi, \eta)$, where X is one of S , D , or T . There are some instances in formulæ (I.1) to (I.3) where singularities occur. Refer to *Okubo* (1991, 1992) for instructions pertaining to their treatment..

I.2.2 EXTENSION TO A COMPLEX FAULT NETWORK

The calculation of the gravity changes is composed of two components: the *steady-state* (or long-term) signal generated by the continual accumulation of strain, modelled as backslip, from the underlying loading plate, i.e., $\vec{U}(x_f) = \vec{V}(x_f)\delta t$; and the sudden release, at time t , of stored seismic strain energy during unstable, co-seismic slip on the fault (i.e., $\vec{U}(x_f, t)$). Here x_f is the location of a single fault segment in the model.

I.2.2.I CALCULATION OF THE STEADY-STATE GRAVITY

The first step in calculating the contribution to the overall gravity from the long term, steady-state component is to artificially create two extensions on the fault segment network at the boundary segments for the driving plate. This is analogous to finite-difference problems where the boundaries are solved by the use of ghost points, which lie outside the computational grid. Similarly, the introduction of our ‘ghost segments’ acts to mitigate anomalous effects at the extreme boundaries on the fault network. The spatial extent of the ghost segments are proportional to a fraction of the average loader plate velocity, $|V|$. More specifically, in the x_1 -direction, spatial extent is proportional to,

$$\frac{V_{x_1}}{|V|}$$

and the spatial extent in the x_2 -direction is proportional to,

$$\frac{V_{x_2}}{|V|}$$

Once the segment geometry and observational grid is set, we then calculate the gravity value which would be observed at each of the

observation grid points on the surface due to the steady-state slip from each segment. We note that in this study there is no cavity filling matter ($\Delta\rho=0$). Applying these changes to (I.1) and (I.3) simplifies the expressions significantly, respectively yielding:

$$\Delta g(x_1, x_2)_f = \left\{ \rho G \left[U_{1_f} S_g(\xi, \eta) + U_{2_f} D_g(\xi, \eta) + U_{3_f} T_g(\xi, \eta) + \right] \right\} \parallel -\beta \Delta h(x_1, x_2)_f \quad (\text{I.4})$$

and,

$$\Delta g^*(x_1, x_2)_f = \left\{ \rho G \left[U_{1_f} S_g^*(\xi, \eta) + U_{2_f} D_g^*(\xi, \eta) + U_{3_f} T_g^*(\xi, \eta) + \right] \right\} \parallel \quad (\text{I.5})$$

where the subscript, f , indicates that this is the result for the contribution of steady-state gravity from a single segment to an observation point located at x . The complete solution for the entire network is the linear sum of these contributions from each segment. Therefore we obtain,

$$\Delta g_{\Sigma_{SS}}(x) = \sum_{f=1}^N \Delta g(x_1, x_2)_f \quad (\text{I.6})$$

and,

$$\Delta g_{\Sigma_{SS}}^*(x) = \sum_{f=1}^N \Delta g^*(x_1, x_2)_f \quad (\text{I.7})$$

for the total gravity and dilatational gravity fields respectively, $N = n+2$ is the number of segments in the network (n), plus two for the ghost segments. The subscript Σ_{SS} indicates the summed steady-state solution for the fault network and the Green's functions are in units of $\mu\text{Gal}\cdot\text{t}^{-1}$ which are then multiplied by the amount of time steady-state slip has occurred, Δt , to yield units of μGal for a given time interval.

I.2.2.2 ELASTIC SLIP GRAVITY FIELD CHANGES

The second contribution, from the purely elastic unstable slip, follows the same method as above with the following exceptions. As this component calculates the gravity from unstable slip from each segment in the network, the use of artificial ghost segments is unnecessary. To be complete in our analysis, we again use (I.4) and (I.5), but now specify that this component is separate from the steady-state contribution by using the notation:

$$\Delta g_{\Sigma_{ES}}(x) = \sum_{f=1}^n \Delta g(x_1, x_2)_f \quad (I.8)$$

and,

$$\Delta g_{\Sigma_{ES}}^*(x) = \sum_{f=1}^n \Delta g^*(x_1, x_2)_f \quad (I.9)$$

for the total gravity and dilatational gravity fields respectively. The subscript Σ_{ES} indicates the summed elastic slip contribution for the fault network.

In the implementation of this component of the gravity signal, we first calculate the response for unit unstable slip, yielding Green's functions with the units of $\mu\text{Gal}\cdot\text{cm}^{-1}$. The elastic slip Green's functions are then multiplied by the modelled slip to obtain a final result with units of μGal .

I.2.2.3 RESULTANT GRAVITY FIELD CHANGES

We now have all the necessary components to find the modelled gravity changes over the fault system. All that remains is to sum the steady-state and elastic slip components of gravity, yielding,

$$\Delta g_{\Sigma_{TOT}}(x) = [\Delta g_{\Sigma_{ES}}(x) + \Delta g_{\Sigma_{SS}}(x)] \quad (I.10)$$

for the total gravity changes from the steady-state and elastic component. We also have

$$\Delta g_{\Sigma_{DIL}}^*(x) = \left[\Delta g_{\Sigma_{ES}}^*(x) + \Delta g_{\Sigma_{SS}}^*(x) \right] \quad (I.II)$$

for the total dilatational component. To obtain the free-air gravity contribution to the signal, i.e., the component of gravity due only to the changes in height, Δh , we subtract (I.II) from (I.IO) as follows:

$$\Delta g_{\Sigma_{FAG}}(x) = \Delta g_{\Sigma_{TOT}}(x) - \Delta g_{\Sigma_{DIL}}^*(x) \quad (I.II)$$

We iterate the calculations (I.IO), (I.II), and (I.III), for each of the observation points. Expressions (I.IO), (I.II), and (I.III) calculate the respective gravity values for a single time-step. We further modify (I.IO), (I.II), and (I.III) to allow for calculating the gravity values over a specified time range by making them functions of time-dependent slip, i.e., $\vec{U} = U(x, t)$. Respectively, this modifies the expressions to:

$$\Delta g_{\Sigma_{TOT}}(x, t) \quad (I.IIIa)$$

$$\Delta g_{\Sigma_{DIL}}^*(x, t) \quad (I.IIIb)$$

$$\Delta g_{\Sigma_{FAG}}(x, t) \quad (I.IIIc)$$

I.3 IMPLEMENTATION

I.3.1 CODE OVERVIEW

As shown in Figure I.2, the implementation of the expressions in (I.III) involves two main Fortran90 programs: `GRAV_GREEN.F90`, and `GRAVITY.F90`, and a visualization routine written in IDL, `GRAVITY90_VIEW.PRO`. The first program to be run is `GRAV_GREEN.F90`, which requires two input files: the fault medium information file, and the fault segment geometry file. `GRAV_GREEN.F90` creates a table of unit

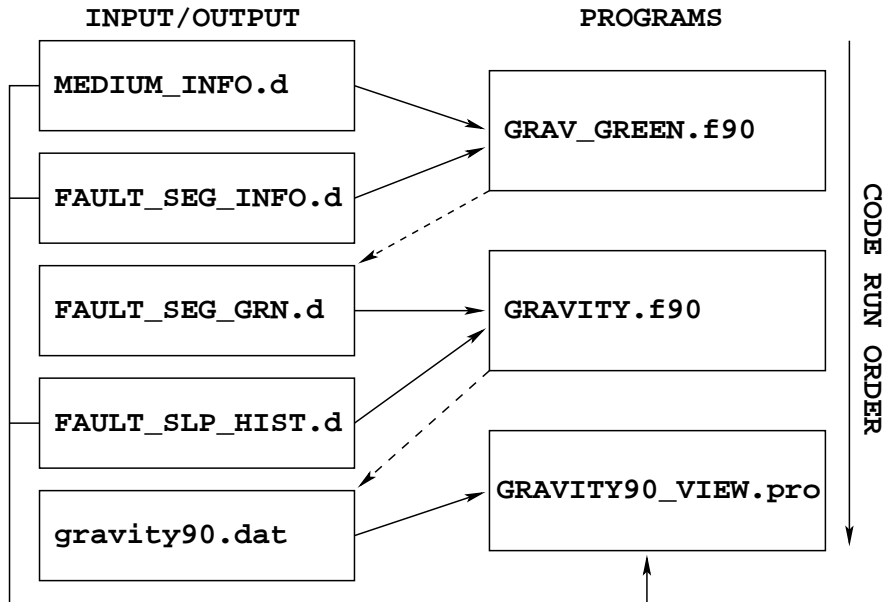


FIGURE I.2: The main flow diagram of the Fortran90 routines and the IDL visualization routine. The left column shows the necessary input files and subsequent output files (dashed lines) used by each program.

gravity Green's function values for the each of the fault segments for each elastic slip component, and a set of steady state values. Once the Green's function values have been tabulated for a specified system, it needs not be called again.

The second program, **GRAVITY.f90**, is a time differencing program which sums the gravity values over a user-specified epoch and outputs the data for use in the IDL visualization routine which further requires a slip history file as its input.

The IDL visualization routine, **GRAVITY90_VIEW.PRO**, is then run to plot the data in order to visualize the data in a user-friendly format. A typical session would proceed as follows.

- I. Run **GRAV_GREEN.f90** to calculate the unit gravity Green's func-

tions

2. Run `GRAVITY.F90` to calculate the total, dilatational, or free-air gravity over a specified time interval
3. Run `GRAVITY90_VIEW.PRO` to view any of the gravity components calculated above

We note that `GRAVITY.F90` is set up to run repeatedly for different gravity calculations in the same system as one may wish to investigate various aspects of the evolution of the gravity signal, i.e., pre-, co-, and post-seismic signals. The user could set up a soft link in their home IDL directory to the output from `GRAVITY.F90`, as well as the inputs used to generate that code. The user would then run `GRAVITY90_VIEW.PRO` after each new time interval is entered, overwriting the `gravity90.dat` file. Each of these aspects will be addressed in more detail below.

1.3.2 `GRAV_GREEN.F90`

To reduce the run time for the overall algorithm, the calculations of the gravity values is split into two routines. The first routine, `GRAV_GREEN.F90`, is used to calculate the unit gravity Green's functions for each of the fault segments for the elastic slip and the steady-state component of slip from the underlying driving plate. The output from this program produces a data file for all necessary subsequent gravity calculations using `GRAVITY.F90`.

1.3.2.1 INPUT AND INITIALIZATION

To generate the gravity Green's function file, the program requires two input files: a file which contains the fault medium information, and

another which contains the fault segment geometry and slip information. Examples of each are provided in the repository (see Figure 1.2).

The fault medium information file contains information used for the medium in which the fault is situated, as well as all other miscellaneous information required by the routine, e.g., number of fault segments, reference latitude and longitude coordinates for the system, boundary and velocity information for the driver-plate, etc., all of which are well documented in the example files. The fault segment information file is essentially a table of values for each of the fault segment's end points, depth to top (and bottom), velocity vector (can be distinct for each segment), and dip angle.

Once the input files are read in, the user creates a distinct output file which will eventually contain the gravity Green's functions, `GRAV_GREEN.F90` then checks to see how the fault segment geometry was defined, using either a latitude-longitude format, or one in kilometres. If the data is provided using the former, the program calls a subroutine to apply a simple Mercator correction to the geometry. This is required as the gravity Green's functions assume a Cartesian elastic half-space for the model. The program also tests several of the input variables provided by the fault medium information file in order to properly calculate both the elastic and steady-state gravity Green's functions. Once the checks have been made, the observation grid on the surface is generated from the information provided in the fault medium information file and writes the observation points to an output file. The observational grid should be set large enough to completely encompass the entire fault system.

1.3.2.2 THE ELASTIC SLIP GREEN'S FUNCTIONS

When calculating the gravity Green's functions (equations (1.1) to (1.3)), unit slip values are used and each component of slip, U_1 , U_2 , and U_3 , is calculated independently of each other so as to allow for different slip magnitudes for each component when calculating the overall result. For example, segment A may have 2.3m of strike-slip motion, and 0.9m of dip-slip motion associated with event 1. Then, several years later, slip again during event 2 with 1.1m of strike-slip motion and 0.5m of dip-slip motion, i.e., each slip event is treated as unique and can have several modes of slip applied for each event. This generates the gravity Green's functions for elastic, unstable slip events and its values are written to the user specified output file at in units of $\mu\text{Gal}\cdot\text{cm}^{-1}$.

1.3.2.3 THE STEADY-STATE SLIP GREEN'S FUNCTIONS

In order to calculate the gravity Green's functions used to approximate an underlying plate loading the system during inter-seismic periods, we follow the same method as above with the following exceptions.

The first step when calculating the steady-state component is to create two extra end segments to remove anomalous boundary effects. The user prescribes in the fault medium file whether the boundaries are in the same orientation (e.g., the San Andreas) or mixed (e.g., the Aleutian mega-thrust). We also need to provide an average surface velocity vector for the underlying plate. The program then automatically calculates the required geometries for the two extra segments.

Secondly, we now assume only one slip vector for each segment. The method still allows for dip-slip, strike-slip, and tensile motion components; however, we now make the assumption that the magnitudes of slip for each component of slip do not change over time. These values are then summed to yield a final value for each point

on the observational grid and written to the output file. For the steady-state gravity values, the units are $\mu\text{Gal}\cdot\text{t}^{-1}$.

1.3.3 GRAVITY.F90

To create the total gravity values in units of μGal , the second Fortran90 routine, GRAVITY.F90, is used. This is a time differencing technique which queries the user for a specified time interval of investigation. The routine works in the following manner.

1.3.3.1 INPUT/OUTPUT

The program asks the user to supply the names of the gravity Green's functions generated by GRAV_GREEN.F90 and the name of the fault slip history file (see Figure 1.2). We note that contained in each of these files are the names of the files for the fault medium and the fault segment geometry and GRAVITY.F90 reads them in automatically. This implies that you must be in the same working directory as that in which you created the gravity Green's functions. For the output, the file writes to a pre-existing file called GRAVITY90.DAT. The name for this file is always the same, so if the user wishes to save the output for later investigation, they must copy this file to a new name in order to prevent overwriting.

Once the input data has been read into the program, the user is asked which time interval they wish to investigate. It is instructive at this stage to provide an example session for the Alaska 1964 earthquake using GRAVITY.F90.

ENTER THE NAME OF THE SLIP HISTORY FILE:

alaska_1964_hst.d

```
ENTER THE NAME OF THE INPUT FILE GRAVITY  
GREENS FUNCTIONS FOR OBSERVATION POINTS.  
alaska_1964_grn.d
```

```
MINIMUM time (yr): 1934.00  
MAXIMUM time (yr): 1984.00
```

We need two dates, a later one
and an earlier one to calculate
the differential offsets.

```
Enter EARLIER date (years)  
1936.0  
Enter LATER date (years)  
1965.0  
Compute another gravity field? (y/n)
```

Here we see the user is queried for the names of the fault slip history file and the gravity Green's function values. The program then reads in the data from each file and presents the user with the maximum and minimum dates that the fault slip history file contains data for. The user can then specify any time interval within those bounds they wish to investigate.

1.3.3.2 THE TIME DIFFERENCING ALGORITHM

Once the time interval has been specified, GRAVITY.F90 then determines the total, dilatational, and free-air gravity values for each of the observations points using the gravity Green's function. This routine determines the sums given in (1.13) and then writes the output to GRAVITY90.DAT.

For the elastic slip component, the total amount of slip for each segment over the time interval specified is summed, and multiplied by the corresponding unit slip gravity Green's functions (given in terms of $\mu\text{Gal}\cdot\text{cm}^{-1}$) to yield a value now in terms of μGal . For the steady-state component of slip, the total time difference specified is used to multiply the steady-state Green's functions (given in terms of $\mu\text{Gal}\cdot\text{yr}^{-1}$) to yield a value in terms of μGal . Once the gravity values for the elastic slip and steady-state values are determined for each of the observation points, the routine sums the values and writes the output to `GRAVITY90.DAT`.

At this stage the user can then visualize the data using `GRAVITY90_VIEW.PRO` while keeping `GRAVITY.F90` running. This prevents constantly re-reading in the data for each calculation of the same data. After the data has been plotted using `GRAVITY90_VIEW.PRO`, the user can investigate another gravity field, and repeat the process as desired. It is important to keep in mind that `GRAVITY90_VIEW.PRO` always uses the most recently generated `GRAVITY90.DAT` file.

1.3.4 `GRAVITY90_VIEW.PRO`

To visualize the data, an IDL program, `GRAVITY90_VIEW.PRO`, has been provided and can be used as pseudo-code for the visualization tool of your choice. To run the IDL program, it is suggested that the user work in a separate directory with soft links to the input files and `GRAVITY90.DAT`. The routine also calls several IDL routines to plot `LATEX` characters, a colourbar, and convert the latitude and longitude values of the observation grid for contouring purposes. All necessary programs are provided in the code repository. Once the links to the necessary data files are created, one can then run `GRAVITY90_VIEW.PRO` at the prompt via the command:

```
IDL> .r GRAVITY90_VIEW.pro
```

The program then queries the user for the gravity field the user wishes to investigate. By choosing the desired letter, the program then generates the plot as an eps file. An example is provided below.

Enter the gravity component you wish to plot:

- [T] = TOTAL gravity change
- [D] = DILATATIONAL gravity component
- [F] = FREE-AIR gravity component

The user also has the option of two plotting styles: a style suitable for print purposes, with a white background; or a style which lends itself to onscreen visualization with a black background. Moreover, the program queries the user for the bounds of the plot area so as to allow for zoomed in viewing of the data once regions of interest have been identified.

1.4 EXAMPLES

1.4.1 THE JOSHUA TREE-LANDERS-HECTOR MINE SEQUENCE

To demonstrate the method in action, we provide two examples to highlight the flexibility of the programs. For our first example, we will look at the evolution of the Joshua Tree-Landers-Hector Mine (JLH) sequence in Southern California. The JLH sequence demonstrates how the method can calculate the changes over time with several elastic-slip events.

The Joshua Tree earthquake occurred on April 23, 1992, with a magnitude of $M_w = 6.1$ (*Bodin et al., 1994*), followed by the Landers earthquake, on June 28, 1994, $M_w = 7.3$ (*Hauksson et al., 1993; Hudnut et al., 1994*), and three hours later, the Big Bear earthquake with a magnitude of $M_w = 6.2$ (*Bodin et al., 1994*). The last earthquake in the

sequence, Hector Mine, occurred on October 16, 1999, with a magnitude of $M_w = 7.1$ (*Freed and Lin, 2001; Simons et al., 2002; Kaverina et al., 2002*).

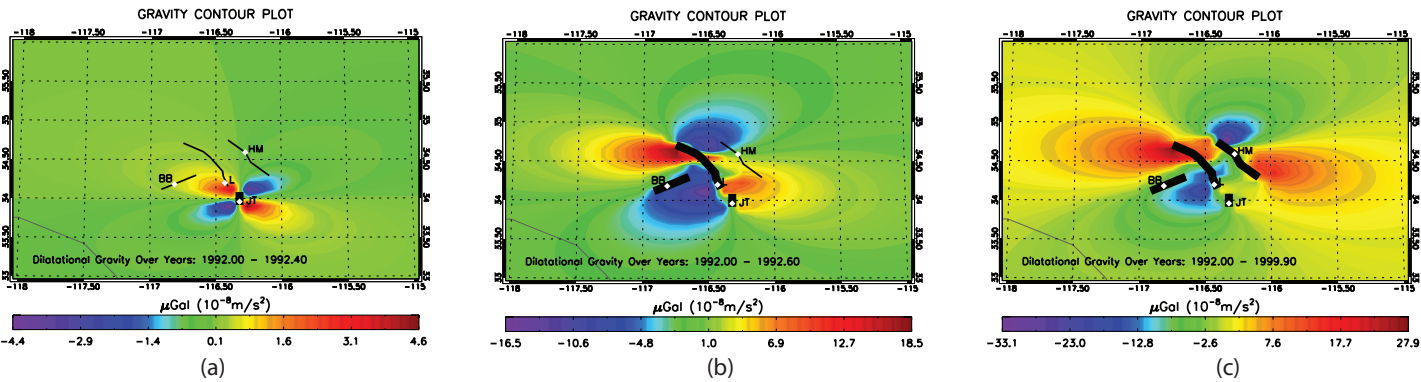
Provided in the Landers example files are the inputs (i.e., fault geometries, slip histories, and magnitudes) used for the sequence. The convention used for assigning the steady-state slip for a strike-slip fault requires that the direction of motion is in the same sense as that which would be used for the elastic-slip on those faults. We provide in Figure 1.3 an example of the method for the sequence earthquakes in Southern California which take place over approximately eight years.

For the strike-slip system, the dilatational component of gravity is the most effective proxy for the gravity field changes which accompany the permanent deformation of the medium from strain accumulation. This is because of the relatively small height changes when compared to the deformation of dip-slip events. We see in Figure 1.3 that the dilatational gravity highs frequently coincide with the locations of the subsequent epicentre locations for each of the unstable slip events. Due to the small rate of inter-seismic strain accumulation within the Mojave fault block, the steady-state component of gravity contributes very little to the overall signal.

1.4.2 THE ALASKA GOOD FRIDAY EARTHQUAKE, 1964

For our second example, we examine the Alaska Good Friday earthquake of 1964. The magnitude $M_w = 9.2$ earthquake occurred on March 27 (March 28, Universal Time), 1964, and deformed approximately 200000km² of the Aleutian trench system in one of the largest recorded earthquakes in history (*Plafker, 1965; Plafker et al., 1994; Wesson et al., 1999*).

This example demonstrates the use of mixed boundaries (the west-



27

FIGURE 1.3: Dilatational gravity plots of a sequence of earthquakes spanning the years 1992–2000: (a) The Joshua Tree earthquake starts the sequence south of the Landers and Big Bear faults. Note the region of dilatational highs from the event. (b) The Landers and Big Bear faults fail within several months following the Joshua Tree event. Dilatational gravity signal high encompasses the middle and southern half of the Hector Mine fault. (c) Hector Mine fails several years later. Thick black lines indicate slipped fault segments, and the white diamonds indicate the epicentre for each event where, JT=Joshua Tree, L=Landers, BB=Bigbear, and HM=Hector Mine. All units are in μGal .

ern most segment is dip-slip, and the southern most segment is strike-slip), as well as the convention used for dip-slip segments when assigning the values for the steady-state motion. This sequence consists of allowing the system to accumulate strain for over twenty years, followed by a large event in 1964.

In dip-slip systems, much of the energy of the driving plate (steady-state component) is used up in bending the plate, whereas in the strike-slip system, approximately half the energy is lost to permanent deformation of the subsurface medium. As such, it is illuminating to view the gravity field which records the gravity signal due to the surface mass that accompanies uplift/subsidence, i.e., the combined free-air and Bouguer effect as given by (1.14).

$$-\beta\Delta h + 2\pi\rho G\Delta h \quad (1.14)$$

In Figure 1.4, we show the slow accumulation of the gravity signal over 26 years prior to the Alaska earthquake, followed by the large slip which occurred in 1964. Note that the label of “Free-Air Gravity” in Figure 1.4, is actually the combined effect given by (1.14).

For dip-slip systems, the steady-state motion is typically in the opposite sense to that of the resultant slip when the system fails. Therefore, the inputs used for the Green’s functions should have the corresponding motion associated with them. Care must be taken when assigning the magnitude of the unstable slip event, as its motion is in the opposite sense to the assigned steady-state motion vectors. To ensure the gravity field has the proper sense of motion for the seismic event, we need to multiply the Green’s functions from the steady-state calculations by -1.0. This is carried out by proper vector assignment within the slip history input file. See the Alaska example files for more details.

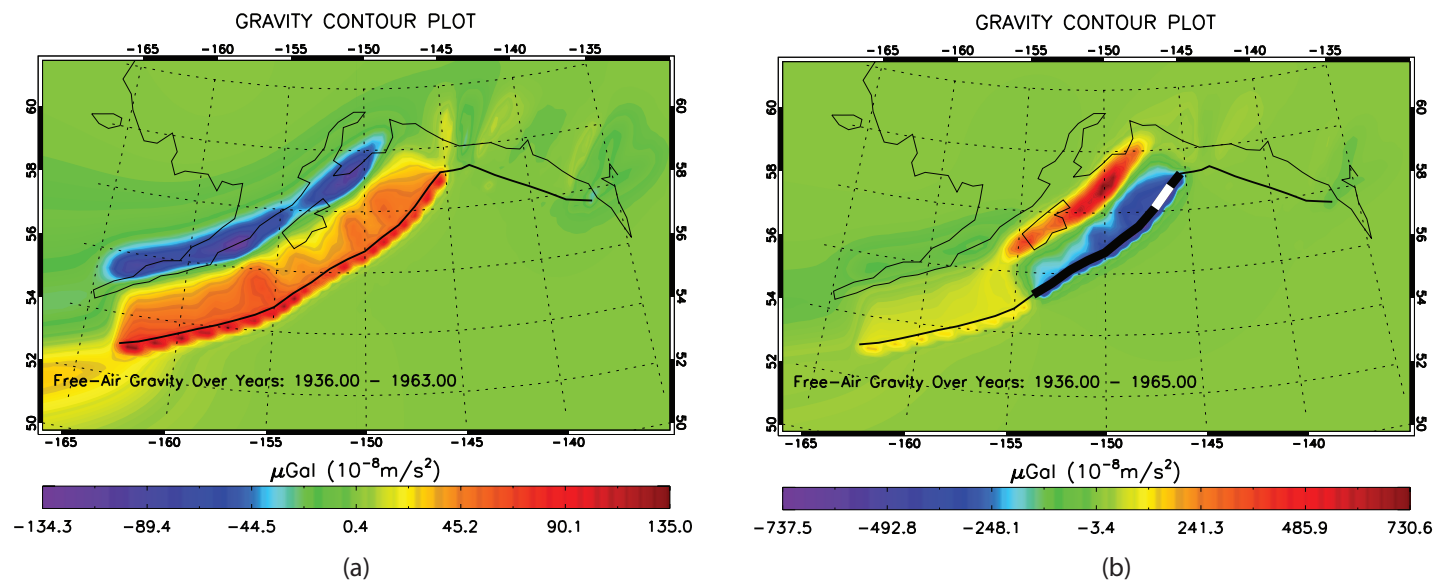


FIGURE 1.4: Gravity plots of the Aleutian mega-thrust system in Alaska, culminating with a model of the Good Friday earthquake of 1964. (a) Free-air gravity signal; a result of the steady-state motion of the underlying driving plate's effects on the topography in the model. (b) The free-air gravity signal after the 1964 event. Note the distribution of the highs and lows are now in the opposite direction. This is expected as the sudden release in subduction systems in the opposite sense to the steady-state motion. All units are μGal .

1.5 DISCUSSION AND CONCLUSION

From the examples provided, we have demonstrated the flexibility of the programs for examining multiple fault systems, with complex geometries. By incorporating realistic fault system geometries, the method allows one to easily visualize regions of potential seismic risk or of academic interest previous unavailable using traditional single fault system methods. Moreover, the range of applications is not limited to any single fault system type; strike-slip and dip-slip systems can be modelled together, or separately. For regions such as southern California, the method provides a complement to Coulomb strain accumulation studies by providing estimates of a directly observable quantity. With the latest incarnations of gravity field instrumentation, the magnitudes are within the range of observable limits when accompanied by appropriate data processing techniques.

The magnitudes of the smaller events are well within the observational range of permanent gravity stations such as Superconducting Gravimeters (*Imanishi et al., 2004*), and portable instruments are now being made with repeatable μGal sensitivities. For dip-slip systems such as the Aleutian mega-thrust system, the method provides quick and easily calculable gravity field estimates which can then be used in TPGA studies (*Song and Simons, 2003*).

The programs have been written to ease the burden on the researcher by allowing for interactive data analysis. Once the fault geometries and slip history are known, data analysis can begin directly. To facilitate the creation of the slip history files, two example Fortran77 routines used to generate the data in a readable format are also provided, but not considered part of the main program structure. It is suggested that the user go through both examples (JLH and Alaska 1964) to familiarize themselves with how the programs work in-

teractively together, i.e., GRAVITY.F90 and GRAVITY90_VIEW.PRO, before attempting their own analysis. Extensive supplementary README files and commenting within the code allow for further clarification, and the modular structure of the routines facilitates extensions of the method with minor effort.

REFERENCES

- Bodin, P., R. Bilham, J. Behr, J. Gomberg, and K. W. Hudnut, Slip triggered on Southern California faults by the 1992 Joshua Tree, Landers, and Big Bear earthquakes, *Bull. Seis. Soc. Amer.*, 84(3), 806–816, 1994.
- Chinnery, M. A., The deformation of the ground around surface faults, *Bull. Seis. Soc. Amer.*, 51(3), 355–372, 1961.
- Chinnery, M. A., The stress changes that accompany strike-slip faulting, *Bull. Seis. Soc. Amer.*, 53(5), 921–932, 1963.
- Freed, A. M., and J. Lin, Delayed triggering of the 1999 Hector Mine earthquake by viscoelastic stress transfer, *Nature*, 411, 180–183, doi: 10.1038/35075548, 2001.
- Hauksson, E., L. M. Jones, K. Hutton, and D. Eberhart-Phillips, The 1992 Landers earthquake sequence: Seismological evidence, *J. Geophys. Res.*, 98(BII), 19,835–19,858, 1993.
- Hayes, T. J., K. F. Tiampo, J. B. Rundle, and J. Fernández, Gravity changes from a stress evolution earthquake simulation of California, *J. Geophys. Res.*, 111, B09408, doi:10.1029/2005JB004092, 2006.
- Hudnut, K. W., et al., Co-seismic displacements of the 1992 Landers earthquake sequence, *Bull. Seis. Soc. Amer.*, 84(3), 625–645, 1994.

- Imanishi, Y., T. Sato, T. Higashi, W. Sun, and S. Okubo, A network of superconducting gravimeters detects submicrogal coseismic gravity changes, *Science*, 306, 476–478, 2004.
- Kaverina, A., D. Dreger, and E. Price, The combined inversion of seismic and geodetic data for the source process of the October 16 1999 $m_W 7.1$ Hector Mine, California, earthquake, *Bull. Seis. Soc. Amer.*, 92(4), 1266–1280, 2002.
- King, G. C. P., R. S. Stein, and J. Lin, Static stress changes and the triggering of earthquakes, *Bull. Seis. Soc. Amer.*, 84(3), 935–953, 1994.
- Li, Q., and M. Liu, Geometrical impact of the San Andreas fault on stress and seismicity in California, *Geophys. Res. Lett.*, 33, L08,302, doi:10.1029/2005GL025661, 2006.
- Okada, Y., Surface deformation due to shear and tensile faults in a half-space, *Bull. Seis. Soc. Amer.*, 75(4), 1135–1154, 1985.
- Okada, Y., Internal deformation due to shear and tensile faults in a half-space, *Bull. Seis. Soc. Amer.*, 82(2), 1018–1040, 1992.
- Okubo, S., Potential and gravity changes raised by point dislocations, *Geophys. J. Int.*, 105, 573–586, 1991.
- Okubo, S., Gravity and potential changes due to shear and tensile faults in a half space, *J. Geophys. Res.*, 97(B5), 7137–7144, 1992.
- Plafker, G., Tectonic deformation associated with the 1964 Alaska earthquake, *Science*, 148(3678), 1675–1687, 1965.
- Plafker, G., L. M. Gilpin, and J. C. Lahr, *The Geology of Alaska, Geology of North America*, vol. G-1, chap. Neotectonic Map of Alaska, Geological Society of America, 1 sheet, scale: 1:2,500,000, 1994.

- Rundle, J. B., and D. D. Jackson, A three-dimensional viscoelastic model of a strike slip fault, *Geophys. J. R. Astro. Soc.*, 49, 575–591, 1977.
- Simons, M., Y. Fialko, and L. Rivera, Coseismic deformation from the 1999 m_W 7.1 Hector Mine, California, earthquake as inferred from InSAR and GPS observations, *Bull. Seis. Soc. Amer.*, 92(4), 1390–1402, 2002.
- Soldati, G., A. Piersanti, and E. Boschi, Global postseismic gravity changes of a viscoelastic Earth, *J. Geophys. Res.*, 103(B12), 29,867–29,885, 1998.
- Song, T.-R. A., and M. Simons, Large trench-parallel gravity variations predict seismogenic behavior in subduction zones, *Science*, 301, 630–633, 2003.
- Wesson, R. L., A. D. Frankel, C. S. Mueller, and S. C. Harmsen, Probabilistic seismic hazard maps of Alaska, Open-File Report 99-36, U.S.G.S., 1999.

CHAPTER 2

GRAVITY CHANGES FROM A STRESS-EVOLUTION EARTHQUAKE SIMULATION OF CALIFORNIA

It is the last lesson of modern science,
that the highest simplicity of
structure is produced, not by few
elements, but by the highest
complexity.

Ralph Waldo Emerson

2.1 INTRODUCTION



URRENTLY, there are numerous fault models which describe the local effects due to topography, stress and strain fields (*Chinnery, 1961, 1963; Rundle and Jackson, 1977; Okada, 1985, 1992*), and the resultant Coulomb stress field of an earthquake after the event has occurred (*King et al., 1994*). Such models have proved useful for a wide variety of applications such as the potential trigger to rupture (*Stein et al., 1994*); however, they lack the ability to change over time as they are not models of the seismic evolution for a fault network with complex geometry. *Smith and Sandwell (2003, 2004, 2006)*,

[†]Reproduced by permission of the American Geophysical Union. Hayes, T. J., K. F. Tiampo, J. B. Rundle, J. Fernández. (2006) Gravity changes from a stress-evolution earthquake simulation of California. *J. Geophys. Res.*, 111(B09408). Copyright 2006 by the American Geophysical Union.

have used known slip histories over approximately the last 200 years to calculate how the Coulomb stress field has changed over time using a more efficient form of the semi-analytic viscoelastic expression's of *Rundle and Jackson* (1977). Such models provide snapshots of the fault system for a given set of input parameters, but they do not dynamically update those parameters in the same manner as a stress-evolution model for the system.

Rundle and Kanamori (1987) recognized that the segment, or asperity, model of an earthquake relies on the individual segment's coseismic stress change and its interaction with neighbouring segments that determine the segment slip. This was developed into a stress-evolution model (*Rundle*, 1988a,b) whereby a fault network for Southern California was allowed to evolve over thousands of years using long range stress interactions to update the system during each time step. While the above model is not currently a forecast, it does exhibit realistic dynamics observed in the Southern California system; its latest incarnation has 650 segments and includes the northern section of the San Andreas (*Rundle et al.*, 2004). *Ward* (2000) developed a time dependent model for 3000 year cycles of earthquakes in the San Francisco Bay Area, and demonstrated the applicability of such models to hazard analysis.

The connection from a time dependent model to a forecast requires the assimilation of observational data into the model in order to properly tune the simulation to present/realistic values. The most common types of observations for the strike-slip San Andreas Fault System (SAF) are: historical earthquakes from paleoseismic data preserved in the rock record (*Brown*, 1990); present day seismic patterns (*Tiampo et al.*, 2002); surface deformation from GPS measurements (e.g., Southern California Integrated GPS Network (SCIGN)); and Interferometric Synthetic Aperture Radar (InSAR) (*Massonnet et al.*, 1993).

The unifying aspect of all these data types is that they are all surface observations: we are left to infer the processes at depth based on the surface expression (e.g., seismicity rates, deformation) of the underlying deterministic dynamical variables at depth (e.g., stress, strain, friction). Rarely is gravity data used for continuous system-level observations.

Okubo (1991, 1992) developed the analytic gravity Green's functions for a fault within an elastic half-space and further suggested that the Bouguer gravity anomaly be used as a proxy for the accumulation of strain at depth. Unlike strain measurements at the surface, gravity measurements made at the surface contain information from all depths of the underlying medium. *Tullis* (1996) demonstrated that the modelled strain rate for Parkfield, California, at depth is below the current detectability limit of strain meters at the surface; a result of the hypocentral depth relative to the strain meter site. Conversely, gravity data can be directly observed and easily collected for system-level resolution through various methods: field campaign, permanent station deployment, or possibly periodic airborne surveys. For strike-slip fault networks, values range from $\sim 10 \mu\text{Gal}$ to $\sim 70 \mu\text{Gal}$; the Scintrex CG-5 Autograv portable gravimeter has standard $1 \mu\text{Gal}$ resolution, and permanent Superconducting Gravimeters (SGs) have nGal resolution. Moreover, large dip-slip earthquakes, such as the Alaska Good Friday earthquake of 1964, or the Hokkaido 2003 earthquake have been shown to be within the range of satellite observations (e.g., Gravity Recovery And Climate Experiment (GRACE)) (*Sun and Okubo*, 2004).

Traditionally, gravity studies of earthquakes have focused on the coseismic changes accompanying an earthquake. Recently, *Song and Simons* (2003) examined the occurrence of large earthquakes in dip-slip systems and their associated free-air gravity anomalies. The study

shows remarkable correlation for the occurrence of seismic events and the associated negative free-air gravity anomalies prior to rupture: a consequence of the energy of the system inducing plate flexure above the locked regions most susceptible to unstable slip. These systems typically produce gravity signals an order of magnitude larger than their strike-slip system counterparts, whose pre-seismic gravity signal is predominantly produced by the resultant dilatation/compression induced by subsurface stress combined with a relatively small component of vertical surface displacement (compared to dip-slip systems). As such, gravity modelling of strike-slip systems has largely been ignored in the literature for long-term observation purposes.

We propose that the long term stress loading of a complex fault network, such as the SAF system, in conjunction with the short term, large magnitude stresses resulting from an earthquake, will produce observable changes in the local gravity signal via the resultant deformation field. Modelling of the gravity signal over large spatial and temporal scales may reveal regions of seismic susceptibility hitherto undetected. Moreover, deviations between the modelled and observed gravity field can highlight regions where previous model assumptions (e.g., friction, medium density) need to be adjusted accordingly. We present here the first attempts at developing a geometrically realistic and time dependent gravity model for the SAF system.

In presenting our analysis, we will briefly describe the *Virtual California* (VC) stress-evolution earthquake simulation of *Rundle* (1988a,b), followed by an outline of the required gravity Green's functions developed by *Okubo* (1991, 1992). We will then present our method of incorporating gravity within the VC simulation, followed by a discussion of the resulting gravity models for the SAF system: the gravity signal from the steady loading of the SAF; coseismic gravity signals; and a 20 year examination, leading to an event similar to the Brawley,

1940, earthquake.

2.2 EVOLUTIONARY EARTHQUAKE MODELS

The development of an earthquake model for prediction and hazard analysis requires a method to update the dynamical input parameters in a physically realistic way, driving the simulation for hundreds to thousands of years (*Rundle*, 1988a; *Ward*, 2000). The need for these evolutionary models is twofold: (i) the deterministic dynamical parameters of the system are inherently unobservable and, (ii) the earthquake dynamics are multi-scaled with varied spatial and temporal ranges. An evolutionary simulation allows one to investigate the multi-scaled dynamics and model the unobservable deterministic parameters in a convenient way.

For earthquake models, the spatial scales range from the grain scale, 1mm to 1cm; the fault zone scale, 1 cm to 100 m; the fault segment scale, 100 m to 10 km; the fault system or network scale, 10 km to 1000 km; and up to the tectonic plate boundary scale, which is in excess of 1000 km. Similarly, we can describe the important temporal scales ranging from the source process time scale, fractions of a second to seconds; to the stress transfer scale, of seconds to years; to the event recurrence time scale, years to thousands of years; up to the fault topology evolution scale, in excess of thousands to millions of years. It becomes evident that, in order to understand earthquake processes over the diverse temporal and spatial ranges, an evolutionary earthquake simulation has many advantages over direct observations alone; in many instances it is the only viable option.

The fundamental and most common observations a time dependent model requires are the inclusion of current seismic and paleoseismic data for recurrence interval and frictional co-efficient estimates; a

fault network geometry which reflects the complexity of the system in a realistic manner; as well as rock mechanics properties of the regional earth structure to estimate the aseismic slip factors as well as the bulk properties of the medium used in the simulation. The inclusion of these data sources is essential to any forecasting method attempting to predict events for a specific region. *Rundle et al.* (2002) refers to this as the data assimilation problem. We note the data collected exists only for a finite number of scales, thus limiting the range of scales available for assimilation into the model. Data which is below the threshold of observational or modelling limits must be treated as a source of noise in the simulation.

2.3 VIRTUAL CALIFORNIA

The *Virtual California* (VC) earthquake simulation (*Rundle*, 1988b; *Rundle et al.*, 2002) is a backslip model whereby the stress accumulation for each segment is generated from the slip deficit (between the loader plate and each fault segment) acquired during each time step as a result of the long term loading plate velocity. The model's primary purpose is to investigate the long range interactions of faults within a complex network and the evolutionary dynamics that drive the system. Its output is a slip history reproducing realistic seismicity patterns as observed in the SAF system. As such, the model concentrates on the fault network, or system, spatial scale, while enabling one to investigate earthquakes along the SAF on the event recurrence time scale.

It is presently impossible to know the current state of the stress and strain fields for California with the accuracy required by a deterministic model. Moreover, the deterministic dynamical expressions of an earthquake system are often unknown and likely non-linear. Instead of attempting to solve the (unknown) non-linear dynamics ab

initio, VC employs a cellular automaton (CA) method whereby the non-linearity of the system is treated via a stochastic algorithm, obviating the need to solve deterministic expressions directly. The VC simulation is modelled such that each fault segment is treated as a cell. The neighbourhood of each cell in VC allows for long-range interactions to take place and is of the order N , where N is the number of segments in the model and thus the number of degrees of freedom in the system. The order- N neighbourhood implies two key assumptions in the model: each segment interacts with all other segments in the system, and the state of each segment itself is also required to properly update the backslip calculation.

The complex fault network geometry of California is represented by 650 fault segments which have been known to fail in the past (*Deng and Sykes, 1997*). Each segment included in the model is approximately 10 km in length, and has a depth of exactly 15 km. Figure 2.1 shows the segments which are used in VC for this study. A complete listing of the of the geometry of the fault segments used in VC for this study is given in, *Rundle et al.* (see 2004, Table 1).

Much of the observational data for use in VC is limited to the fault network and recurrence interval time scales and is subsequently averaged where appropriate. This allows more direct assimilation of the observational data into the model. The process of data assimilation for the VC simulation has been extensively discussed in the works of *Rundle et al.* (2000, 2002, 2004) and the reader is referred to those articles for a complete discussion.

2.3.1 THE SIMULATION ALGORITHM

Once the data assimilation is complete, we are ready to begin the simulation process. The simulator consists of three main codes, followed

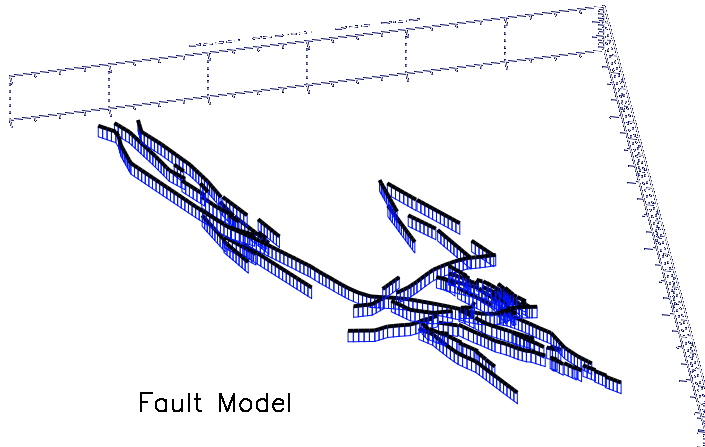


FIGURE 2.1: The 650 fault segments display the complexity of the fault network geometry.

by visualization routines. The first two routines generate the input files for the main earthquake simulator. After the simulator has been run for several thousands of years, its output can then be studied via a suite of visualization routines, or subsequently used to create the gravity evolution for the SAF system.

2.3.1.1 THE MAIN SIMULATOR ALGORITHM

The main earthquake simulator is the CA algorithm and is the *transition function* (see Weisbuch, 1991) which updates each segment from its state at t to its new state at $t + \delta t$. In general, the transition function contains the rules for how each cell is updated during each step; the transition function can vary from the simple rules outlined in Conway's Game of Life, to the more complex algorithm outlined below.

We start by updating the slip deficit, $\phi(x, t)$, using the relation,

$$\phi(x, t) = s(x, t) - V(x)\delta t \quad (2.1)$$

where $s(x, t)$ is slip, V is our long term slip rate. We then use the previously calculated kinematic stress Green's interaction coefficients, $\mathbf{T}_{ij}^{kl}(x - x')$, to update the normal stress, $\chi(x, t)$, and shear stress, $\sigma_{xy}(x, t) = \tau_{xy} + \tau_{xy}^{bac}$, where τ_{xy} is the component of stress each segment contributes to every other segment due to the new value of $\phi(x, t)$, and τ_{xy}^{bac} is a background component stress common to the system. We then calculate the Coulomb Failure Function (CFF) in the typical fashion via,

$$CFF(x, t) = \sigma_{xy}(x, t) - \mu_s \chi(x, t) \quad (2.2)$$

At this stage, due to the stress increase from the underlying loading plate there is a fraction of stable, or aseismic, slip which is released, and characterized by the parameter α . We use a discretized form of the Coulomb friction law below:

$$\frac{\Delta s(x, t)}{\Delta t} = \frac{\Delta \sigma}{K_L} [\alpha + \delta(t - t_F)] \quad (2.3)$$

In (2.3), $\Delta \sigma = \sigma(x, t) - \sigma^R(V)$ is the velocity-dependent stress drop associated with the aseismic slip, and $V = V(x)$. K_L is the stress-drop stiffness for each fault segment which is inversely proportional to each segment's average slip rate. K_L represents the loader plate spring constant in the model. We further note that t_F is any time when the condition $\sigma(x, t_F) = \sigma^F(V)$ is met, i.e., the value of stress when failure occurs. The variables, $\sigma^R(V)$ and $\sigma^F(V)$ can be further parameterized by the coefficients of friction, i.e., $\sigma^R(V) = \mu_k \chi(x, t)$ and $\sigma^F(V) = \mu_s \chi(x, t)$. Having updated the system with stable slip,

we once again update the stress for the entire system via $\mathbf{T}_{ij}^{kl}(x - x')$ and calculate $CFF(x, t)$ for each segment using (2.2).

The simulation is run as described above, incrementing the stress on the system due to the loader plate velocity until failure occurs on a segment(s). Failure occurs when the condition $CFF(x, t) \geq 0$ is met.

Once the CFF criterion for failure has been met on one segment, we then enter into the failure loop which consists of a series of parallel Monte Carlo Sweeps (mcs). During the first mcs we allow unstable slip of magnitude,

$$\Delta s(x, t) = \frac{\sigma(x, t) - \mu_k \chi(x, t)}{K_T} (1 + \rho) \quad (2.4)$$

for each site which meets the failure criterion. The value ρ is a randomly generated variable whose probability density function is uniformly distributed over the interval (± 0.1) . This allows for up to 10% of random over-/undershoot of slip on the fault. Note here we now use the total spring constant, $K_T = K_L + K_p$, where K_p is interpreted as the spring constant for each segment with all other segments in the model. Physically, this is done to allow the failing sites to transfer stress to all of the segments in its neighbourhood, i.e., the entire fault network. The stress is once again transferred via $\mathbf{T}_{ij}^{kl}(x - x')$ using the same procedure as before to update the stresses from the backslip calculation. This ends the first mcs.

We must now determine whether or not any other segments are now at failure ($CFF(x, t) \geq 0$) due to the stress acquired from the unstable slip in the first mcs. Slip and stress are once again updated as above and repeated until the end of the mcs procedure, when no new sites are at failure. Healing on a segment is only allowed once all of the slips have been updated. At this point we exit the failure algorithm and return to the main routine. Time is updated from t to

$t + \delta t$ and we repeat the entire process until a maximum time, $t = t_M$ (defined by the user), is reached. For typical runs of the simulation we set $t_M = 5000\text{yr}$. The above procedure was used for all runs used in this study.

Using the Virtual California earthquake simulator, we are able to create realistic earthquake evolutions for California over thousands of years. From the slip histories created, one can then model how other aspects of the system evolve. Previous studies that use known slip histories of the SAF system have focused on generating maps of the time dependent Coulomb stress field (*Deng and Sykes, 1997; Smith and Sandwell, 2003*), or surface deformations that are readily captured by the densely deployed GPS stations throughout California (e.g., SCIGN). This study will develop a model to show the spatial evolution of the gravity signal for California using the simulated earthquake histories generated by VC.

2.4 GRAVITY GREEN'S FUNCTIONS

In practise, the true deterministic state variables (e.g., $\sigma(x, t)$) which drive the system dynamics are unobservable at the surface. What is recorded are the surface dynamics resulting from the evolution of the underlying state variables (*Rundle et al., 2001*). One variable whose surface expression is a record of the processes at all depths is gravity. Accordingly, *Okubo (1992)* suggests that one can use the Bouguer gravity anomaly as a proxy for strain accumulation at depth.

By incorporating the Green's functions for gravity changes into VC, we acquire the ability to model the evolution of the gravity changes over extended time scales. The expectation is that the accumulation of the long-period gravity signals may be observable through field mapping excursions. *Sun and Okubo (2004)* have shown that large

subduction zone earthquakes, Alaska (1964,2002) and Hokkaido (2003), are within the expected observable limits of the Gravity Recovery and Climate Experiment (GRACE) satellites. These large earthquakes are associated with short period signals with a temporal range of 100 s to 10 000 s, much smaller than the evolution of the slow strain build up of 100 yr to 10 000 yr. The long term loading plate over time that drives the system will also contribute a significant component over long integration times. We will demonstrate that the gravity signals generated by a strike-slip system, such as the SAF system, are within the range of current portable and permanent field instruments.

The Green's function solutions of *Okubo* (1991, 1992) allow one to calculate the total gravity change, free-air gravity change, or the dilatational changes for a rectangular fault within a half-space with arbitrary dip. Since the fault segments used in VC are strike-slip rectangular fault planes within an elastic half-space, as described in Section 2.3, the inclusion of gravity changes within VC is a natural extension of the simulator's applicability. This section outlines those required expressions of *Okubo* (1991, 1992) by which gravity within an elastic half-space is calculated for our model.

2.4.1 POINT SOURCE POTENTIAL CHANGES

The analytical solutions of strain and deformation in a half-space were developed by *Steketee* (1958a,b); *Press* (1965), then further extended by *Chinnery* (1961, 1963), *Maruyama* (1964), and *Mansinha and Smylie* (1971) to include different fault types (e.g., strike-slip, dip-slip). These were finally unified into a single notation and coordinate system by *Okada* (1985, 1992). In order to find the co-seismic gravity Green's functions, *Okubo* (1991, 1992) calculates the potential changes due to a deformation field and then takes the vertical derivative of those solutions to obtain

the gravity values.

The first component *Okubo* (1992) describes is the change in the potential which occurs solely because of density perturbations in the underlying medium. Physically this can produce dilatational or compressional regimes (i.e., the Bouguer anomaly), and they are described by $-\rho[\nabla \cdot \mathbf{u}(\mathbf{r}'; \xi_3)]$. We will refer to this type of potential change as the *dilatational* component of the total potential field. The second change in the potential arises from the mass displaced vertically Δh from the source. This is and denoted as $\Delta\phi$. We will refer to this component as the *free-air* component of the total gravity. There can also be a component of potential changes associated with the generation of a cavity filled with new material of density ρ' ; this is the *cavitation* component of the potential and will not be investigated in this study.

2.4.2 GRAVITY CHANGE FOR A FINITE FAULT

To find the solution for a finite fault plane, simplify by finding the changes observable at the surface with a source located at $\xi \equiv \xi_3$. Then the slip vector, $\Delta s = (U_1, U_2 \cos \delta - U_3 \sin \delta, -U_2 \sin \delta - U_3 \cos \delta)$, is defined for a rectangular fault with a length L , width W , dip angle $0 < \delta \leq \pi/2$, and depth d . Figure 2.2, shows the relationship among these variables. Positive values of U_1 , U_2 , U_3 , correspond to left-lateral slip, thrusting slip, and tensile motion respectively; $\delta = \pi/2$ corresponds to a purely strike-slip fault.

Using the coordinate system in Figure 2.2, *Okubo* (1992) obtains for the coseismic change in gravity, Δg , of a finite fault plane evaluated

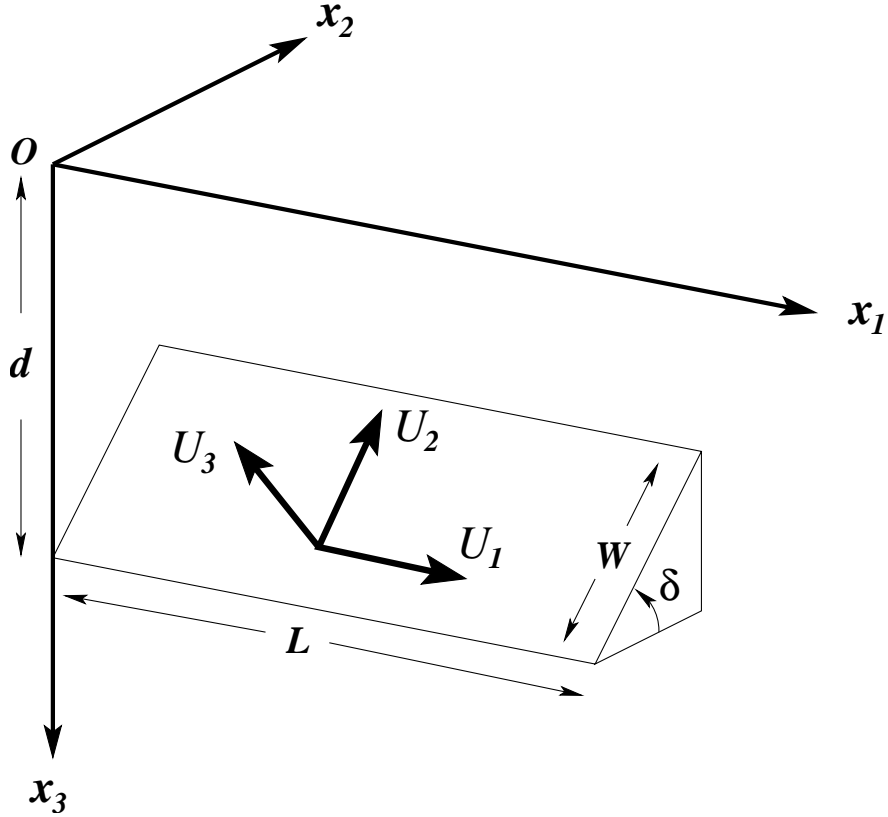


FIGURE 2.2: The coordinate system with origin O , and the source model geometry used for the calculation of the gravity Green's functions. See text for symbol meanings. Modified after *Okubo* (1992).

at the surface, i.e., $x_3 = 0$, a solution of the form,

$$\Delta g(x_1, x_2) = \left\{ \rho G \left[U_1 S_g(\xi, \eta) + U_2 D_g(\xi, \eta) + U_3 T_g(\xi, \eta) \right] + \Delta \rho G U_3 C_g(\xi, \eta) \right\} - \beta \Delta h(x_1, x_2) \quad (2.5)$$

Where we have used the double vertical notation of *Chinnery* (1961). The free-air gravity gradient is given by $\beta = 0.309e^{-5} \text{m/s}^2$, $\Delta \rho$ is the difference in density between the cavity filling matter and the original medium, i.e., $\Delta \rho = \rho' - \rho$. The functions, $S_g(\xi, \eta)$, $D_g(\xi, \eta)$,

$C_g(\xi, \eta)$, and $T_g(\xi, \eta)$ are gravity Green's function contributions from the strike-slip, dip-slip, cavity filling, and tensile components respectively. For our study, we only require the Green's function for the strike-slip case which is given by:

$$S_g(\xi, \eta) = \frac{q \sin \delta}{R} + \frac{q^2 \cos \delta}{R(R+\eta)} \quad (2.6)$$

and the function $\Delta h(x)$ in (2.5), evaluated at $x = (x_1, x_2)$, records the elevation change and is given by *Okada* (1985) as,

$$\Delta h(x) = \frac{1}{2\pi} \left[U_1 S_b(\xi, \eta) \right] \parallel \quad (2.7)$$

$$S_b(\xi, \eta) = \frac{\bar{d}q}{R(R+\eta)} + \frac{q \sin \delta}{R+\eta} - I_4 \sin \delta \quad (2.8)$$

where,

$$\begin{aligned} R &= \sqrt{\xi^2 + \eta^2 + q^2} \\ q &= x_2 \sin \delta - (d - x_3) \cos \delta \\ \bar{d} &= \eta \sin \delta - q \cos \delta \\ \bar{y} &= \eta \cos \delta + q \sin \delta \end{aligned}$$

and finally,

$$I_4(\xi, \eta) = (1 - 2\nu) \left[\log(R + \bar{d}) - \sin \delta \cdot \log(R + \eta) \right] \sec \delta$$

where ν is the Poisson ratio and is set to 0.25 in this study.

For the gravity change free from the effect of the vertical displacement of the ground, $\Delta h(x_1, x_2)$, *Okubo* (1992) provides the following expression,

$$\begin{aligned} \Delta g^*(x_1, x_2) &= \left\{ \rho G \left[U_1 S_g^*(\xi, \eta) + U_2 D_g^*(\xi, \eta) + U_3 T_g^*(\xi, \eta) \right] \right. \\ &\quad \left. + \Delta \rho G U_3 C_g(\xi, \eta) \right\} \parallel \quad (2.9) \end{aligned}$$

where, once again, we require only the strike-slip component, viz.,

$$S_g^*(\xi, \eta) = I_4 \sin \delta \quad (2.10)$$

There are some instances in formulæ(2.5) to (2.10) where singularities occur. Refer to *Okubo* (1991, 1992) for instructions pertaining to the treatment of the cases when $\cos \delta = 0$, $\xi = 0$, $q = 0$, or $R + \eta = 0$; as well as a complete description of the derivations. The outline shown here presents only those aspects of the calculation of the gravity Green's function solutions pertinent to our problem.

2.5 VIRTUAL GRAVITY

The solutions given by (2.5) to (2.10) have proved useful in a wide variety of applications. These expressions assume a single fault plane whose geometry does not change over long distances; a reasonable approximation over regions of several tens of kilometres. However, the assumption ceases to be realistic at the fault network scale where asperities in the medium cause the fault geometry to deviate and develop splays and sub-faults as observed in the SAF system. We can obviate this inherent limitation by breaking up the faults in the SC fault network into the ‘segments’ used in the VC simulation and then use a linear sum of their solutions for each segment. Doing so allows us to maintain confidence in the validity of using (2.5) to (2.10) over an extended region with multiple faults that exhibit complex geometries. This section outlines the method by which this was achieved now that the necessary components of the theory have been established.

2.5.1 OVERVIEW OF VC’s GRAVITY CALCULATION

In calculating the changes in the gravitational field we wish to adhere to several criteria. The first is the principle of least interference we

apply by developing a method which imposes the least amount of modification to the main earthquake simulator. Moreover, it removes any subjectivity calculating the gravity from multiple faults over a large network. An ancillary goal was to develop a modular algorithm in order to allow subsequent modification for future endeavours with ease. We applied all these criteria in the following way.

2.5.2 THE GRAVITY GREEN'S FUNCTIONS ROUTINE

The calculation of the gravity changes from the slip histories generated by VC is comprised of two components: the *steady-state* (or long-term) signal generated by the continual accumulation of backslip from the underlying loading plate with magnitude, $V(x)\delta t$; and the sudden release of strain energy during unstable slip on the fault (i.e., $\Delta s(x, t)$) as described by (2.4) in Section 2.3. Accordingly, the first step was to have the *Virtual Gravity* routine (VG) extract: the slip histories generated by VC; the fault network geometry; and the average fault segment velocities as estimated in the data assimilation process. Once these data were assimilated an observation grid of 10 000 points was created to cover all 650 fault segments in the model.

2.5.2.1 CALCULATION OF THE STEADY STATE GRAVITY

The first step in calculating the contribution to the overall gravity from the long term, steady-state component is to artificially create two extensions on the fault segment network at the northern-most and southern-most segments in the network. This is analogous to finite-difference problems where the solution cell on the boundary is solved by the use of ghost points, which lie outside the numerical grid, in order to properly calculate the dynamics on the boundaries. Similarly, the introduction of our ‘ghost segments’ acts to mitigate

anomalous effects at the extreme boundaries on the fault network. The spatial extent of the northern and southern extensional segments are proportional to a fraction of the average loader plate velocity, $|V|$. More specifically, in the x_1 -direction, spatial extent is proportional to,

$$\frac{V_{x_1}}{|V|}$$

and the spatial extent in the x_2 -direction is proportional to,

$$\frac{V_{x_2}}{|V|}$$

Once the segment geometry and observational grid is set, we then calculate the gravity value which would be observed at each of the 10 000 grid points on the surface due to the steady-state slip from each segment. We note that in this study we can make the following simplifications: all slip motion is strike-slip, so that $\Delta s(x, t) = (U_1, 0, 0)$, $\delta = \pi/2$, and there is no cavity filling matter, $\Delta \rho = 0$. Applying these changes to (2.5) and (2.9) simplifies the expressions significantly, respectively yielding:

$$\Delta g(x_1, x_2)_f = \left\{ \rho G \left[U_1 S_g(\xi, \eta) \right] \right\} \| - \beta \Delta h(x_1, x_2) \quad (2.11)$$

and,

$$\Delta g^*(x_1, x_2)_f = \left\{ \rho G \left[U_1 S_g^*(\xi, \eta) \right] \right\} \| \quad (2.12)$$

where the subscript, f , indicates that this is the result for the contribution of steady-state gravity from a single segment to an observation point located at $r = (x_1, x_2, 0)$. The complete solution for the entire network is the linear sum of these contributions from each segment. Therefore we obtain,

$$\Delta g_{\Sigma_{SS}}(r) = \sum_{f=1}^N \Delta g(x_1, x_2)_f \quad (2.13)$$

and,

$$\Delta g_{\Sigma_{SS}}^*(r) = \sum_{f=1}^N \Delta g^*(x_1, x_2)_f \quad (2.14)$$

for the total gravity and dilatational gravity fields respectively, N is the number of segments in the network, and the subscript Σ_{SS} indicates the summed steady-state solution for the fault network.

Now that we have developed the expressions for the entire network, we are able to find the gravity from the steady-state slip in California. To do so we must calculate U_i for (2.11) and (2.12); the strike-slip component of the slip vector $\Delta s(x)$. As this value of slip is constant over all time steps we use,

$$U_i^{SS} = \Delta s(x)_f = V(x)_f \delta t \quad (2.15)$$

to find the gravity contribution of steady-state slip per unit time step for each fault segment. We note that in the implementation of the algorithm that the output from this step is in units of $\mu\text{Gal}\cdot\text{t}^{-1}$. These Green's functions for a unit response are then multiplied by the appropriate amount of time under investigation to yield a change in μGal .

2.5.2.2 THE ELASTIC CONTRIBUTION TO GRAVITY

The second contribution, from the purely elastic unstable slip, follows the same method as above with the following exceptions. This component calculates the gravity from unstable slip from each segment in the network, thus the use of artificial ghost segments is unnecessary. To be complete in our analysis, we again use (2.11) and (2.12), but now specify that this component is separate from the steady-state

contribution by using the notation:

$$\Delta g_{\Sigma_{ES}}(\mathbf{r}) = \sum_{f=1}^N \Delta g(x_1, x_2)_f \quad (2.16)$$

and,

$$\Delta g_{\Sigma_{ES}}^*(\mathbf{r}) = \sum_{f=1}^N \Delta g^*(x_1, x_2)_f \quad (2.17)$$

for the total gravity and dilatational gravity fields respectively. The subscript Σ_{ES} indicates the summed elastic slip contribution for the fault network.

The main difference from the steady-state component is that we are now relying on the time dependent variable slip $\Delta s(\mathbf{x}, t)$ as given by (2.4). In other words, we set the strike-slip component of the slip vector in (2.11) and (2.12) to,

$$U_i^{ES} = \Delta s(\mathbf{x}, t)_f = \left[\frac{\sigma(\mathbf{x}, t) - \mu_k \chi(\mathbf{x}, t)}{K_T} (1 + \rho) \right]_f \quad (2.18)$$

for the elastic slip case. In the implementation of this component of the gravity signal, we first calculate the response for unit unstable slip, yielding Green's functions with the units of $\mu\text{Gal}\cdot\text{m}^{-1}$. The Green's functions are then multiplied by the modelled slip output by VC to obtain a final result with units of μGal .

2.5.2.3 RESULTANT GRAVITY FIELD CHANGES

We now have all the necessary components to find the modelled gravity changes over the SAF system using the VC stress-evolution earthquake simulation. All that remains is to sum the steady-state and elastic slip components of gravity, yielding,

$$\Delta g_{\Sigma_{TOT}}(\mathbf{r}) = [\Delta g_{\Sigma_{ES}}(\mathbf{r}) + \Delta g_{\Sigma_{SS}}(\mathbf{r})] \quad (2.19)$$

for the total gravity changes from the steady-state and elastic component. We also have,

$$\Delta g_{\Sigma_{DIL}}^*(r) = [\Delta g_{\Sigma_{ES}}^*(r) + \Delta g_{\Sigma_{SS}}^*(r)] \quad (2.20)$$

for the total dilatational component. To obtain the only free-air gravity contribution to the signal, i.e., the component of gravity due only to the changes in height, Δh , we subtract (2.20) from (2.19) as follows:

$$\Delta g_{\Sigma_{FAG}}(r) = \Delta g_{\Sigma_{TOT}}(r) - \Delta g_{\Sigma_{DIL}}^*(r) \quad (2.21)$$

We iterate the calculations (2.19), (2.20), and (2.21), for each of the 10 000 observation points, and then we can examine the gravity changes on the fault network.

2.6 RESULTS

2.6.1 THE STEADY-STATE GRAVITY SIGNAL

Figures 2.3, 2.4, and 2.5 models how the gravity accumulates from only the steady-state loading over a five year interval. The complex geometry of the fault network is interpreted to be the main mechanism by which the spatial extent of the gravity is affected. The background plate velocity of each segment drives the magnitude of the signal.

The total gravity changes range from $2.18 \mu\text{Gal}$ to $-1.11 \mu\text{Gal}$ for the five year period, and the dilatational component of the gravity signal has a range of $1.39 \mu\text{Gal}$ to $-2.92 \mu\text{Gal}$. The free-air gravity values contain the largest magnitude signal, with a range of $5.01 \mu\text{Gal}$ to $-2.48 \mu\text{Gal}$. These values are at the current limits of portable instruments, and within the range of long-term permanent recording devices. Over a ten year period the spatial extent of the steady-state component (not shown) is remarkably similar to the five year case. The

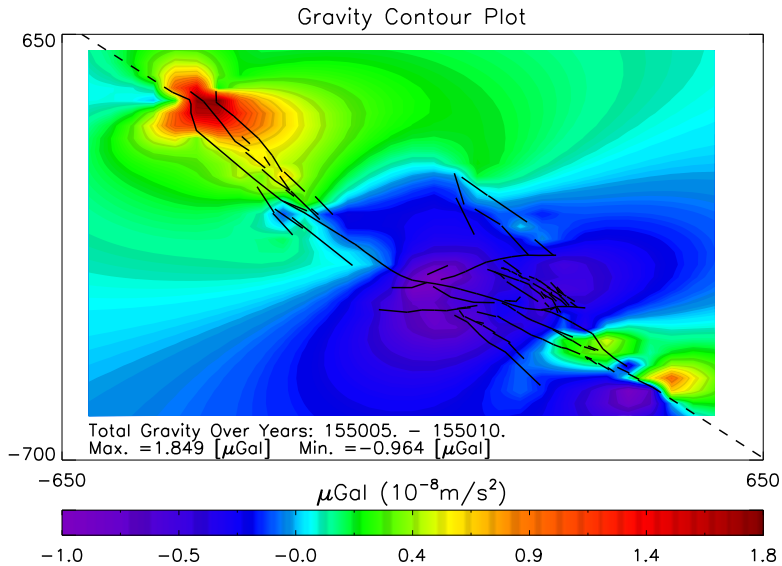


FIGURE 2.3: Gravity plot of the steady-state field showing the total gravity. The black lines are the 650 fault segments used in this study.

main difference is that the magnitude of the signal is approximately double. This result was expected as the stochastic unstable slips in the system provide the largest variability of the gravity signal in the elastic half-space used here.

2.6.2 LARGE EVENT GRAVITY SIGNALS

We now examine the gravity signals generated for large slip events such as the 1906 San Francisco earthquake and the 1857 Fort Tejon earthquake. Figure 2.6 shows an event similar to the San Francisco earthquake of 1906. It is important to remember that the model's only input are the fault geometry and the assimilated coarse grained variables. The event in Figure 2.6 arises solely from the evolutionary dynamics and the long-range stress interactions in the simulation and

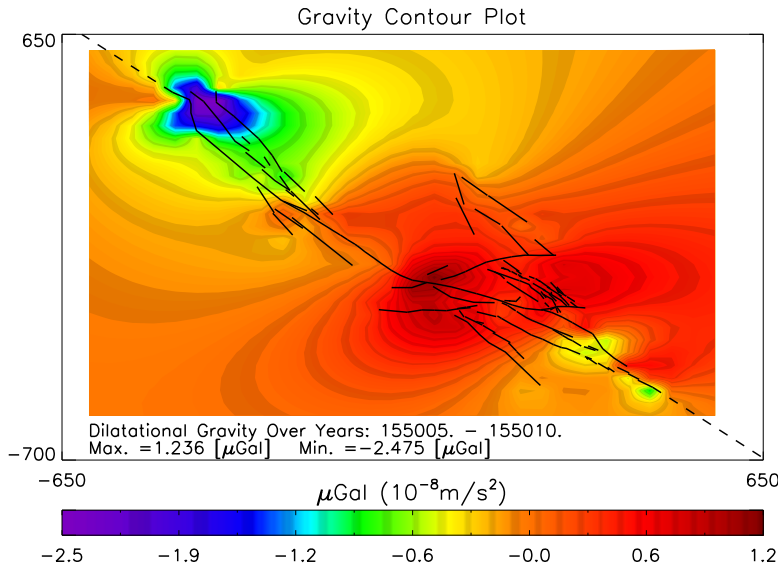


FIGURE 2.4: Gravity plot of the steady-state field showing the dilatational gravity.

is not prescribed to fail in the manner shown.

The most interesting spatial signal in Figure 2.6 emerges from the dilatational component of gravity. Here we observe a small, but non-negligible effect of the steady-state signal imposing a slight trend. Moreover, the effect of having the slip occur on multiple segments (thick black lines) as well as the complex geometry affects the shape of the signal. For a perfectly straight fault, one would expect to see an antisymmetric ‘butterfly’ distribution of gravity (see *Okubo, 1992*, Figure 4(b)). The effect of slip in the Concord-Green Valley area has both mitigated and amplified the gravity signal in unpredicted ways north-east of the region. The dilatational gravity signal from this event ranges from $43.92 \mu\text{Gal}$ to $-49.08 \mu\text{Gal}$, and the free-air component has similar magnitudes. The elevation changes recorded by the free-air component play a significant role in the gravity signal close to the

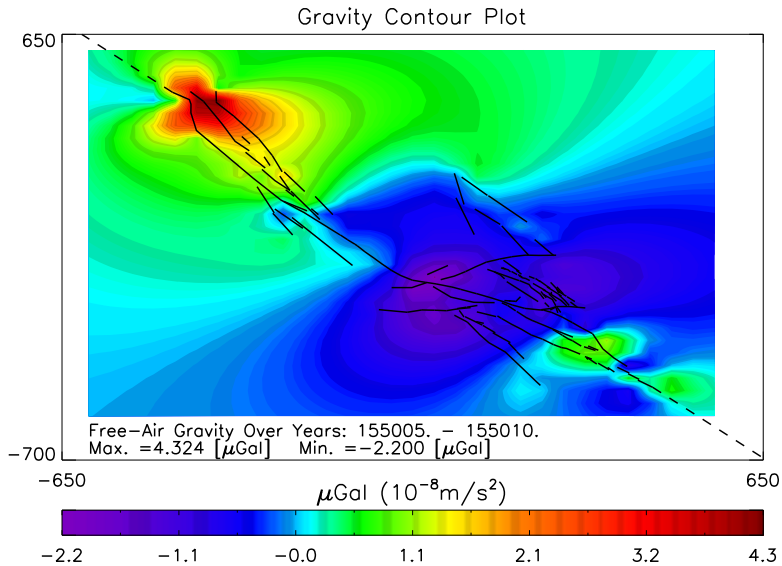


FIGURE 2.5: Gravity plot of the steady-state field showing the free-air gravity.

rupture and are in the opposite sense to the dilatational signal.

For another large event from the simulation, similar to the 1857 Fort Tejon event, we observe even more significant contributions to the gravity signal shape from the fault network geometry. In this case we have very few segments that slip with significant magnitude that are not a part of the main event. This allows us to examine the effect of the contribution almost exclusively from the complex geometry. Here we see how the ‘Big Bend’ of the San Andreas distorts the symmetry of the signal in interesting ways. The large magnitude signals, both positive and negative, lie on the eastern portion of the fault. Conversely, on the western side of the bend, we observe a relatively smaller gravity signal, both positive and negative. Here, the stronger signal, $50.34 \mu\text{Gal}$ to $-59.85 \mu\text{Gal}$, reflects the larger modelled slip magnitudes compared to the 1906 San Francisco type event segment

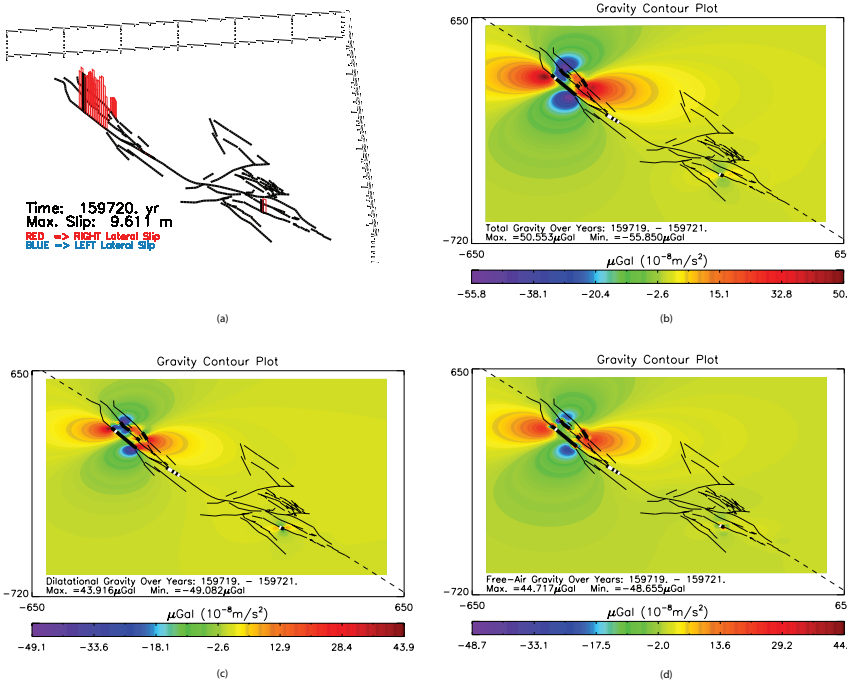


FIGURE 2.6: Gravity plots of a large event similar to the San Francisco earthquake of 1906: (a) The total elastic slip from each segment that slipped in the simulation. The height of the bars is proportional to the amount of slip for each segment, and the black bar(s) indicate an initiator site, i.e., hypocenter. Figures (b) to (d) are the total gravity signal, the dilatational component, and the free-air components respectively. The thick black lines indicate segments that slipped during the interval modelled; the thick white lines indicate which segments were initiators, i.e., segments which failed during the first MCS.

slips. The total gravity values (not shown) range from $84.17 \mu\text{Gal}$ to $-64.68 \mu\text{Gal}$. Another significant result was the location of the initiator segment (i.e., the vertical black bar in Figure 2.7(a)) for the Tejon sequence. The initiator segment is located at the ‘Big Bend’ of the San Andreas fault; the same location shows an anomalous high in the dilatational steady-state gravity signal in Figure 2.4. The dilatational high in the steady-state signal reflects the locally increased density of the subsurface as a consequence of a compressional regime under continual loading.

2.6.3 GRAVITY EVOLUTION OF A MODERATE-SIZED EVENT

We next examined a smaller event, similar to Brawley 1940, generated by the model. Here we examine the 15 years of the accumulated gravity signal prior to the Brawley event and the event itself. This allows us to observe the evolution of the gravity signal in the region in five year time steps and identify regions of anomalous stress loading implied by the gravity changes.

Figure 2.8 shows the slip modelled for the event which occurred in the model year 155450. Figures 2.9 to 2.12 show the gravity signal which develops over time starting in year 155435, and ending with the rupture of the Brawley segments in year 155450. Early on in the sequence (Figure 2.9), the signal is dominated by the steady-state signal for the SAF system with components from small magnitude elastic slip events.

In Figure 2.10, we see a small dilatational signal increase, $\sim 2 \mu\text{Gal}$, for the Imperial Valley/Salton Sea region as well as the Santa Monica and Santa Cruz Island splay resulting from the rupture of the Coronado Bank fault segments. Vertical deformation plays a significant role in accommodating the increased stress as demonstrated by

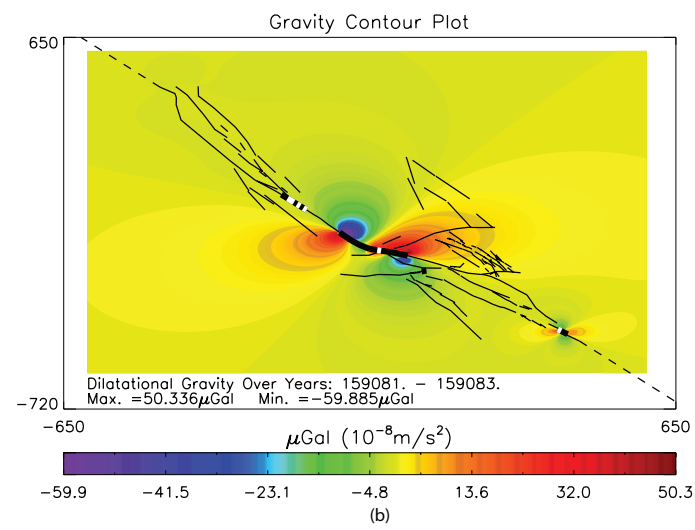
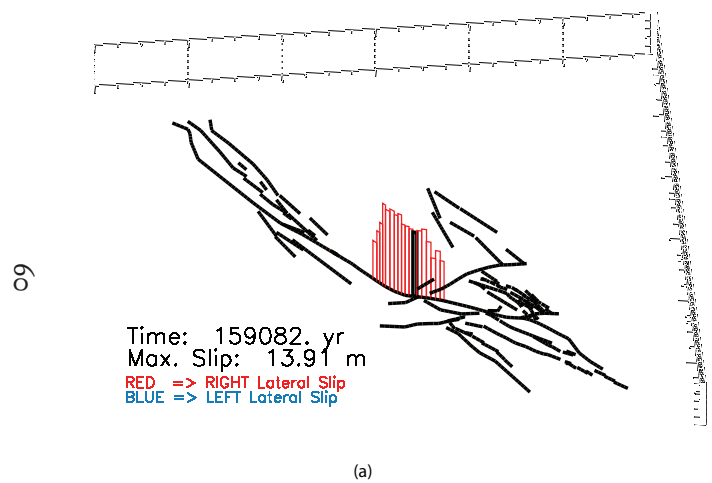


FIGURE 2.7: Gravity plots of a large event similar to the Fort Tejon earthquake of 1857: (a) The total elastic slip for each segment that slipped in the simulation; (b) is the dilatational gravity signal. The key is the same as in Figure 2.6.

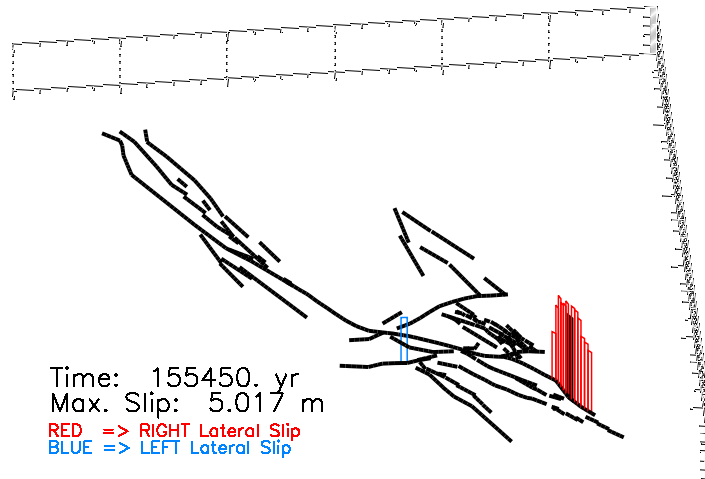


FIGURE 2.8: Modelled slip for an event at Brawley.

the total gravity signal. Figure 2.11 shows the total gravity signal and maps out how the stress is accommodated in the region by both the subsurface dilatational regime as well as vertical deformation. Clearly, Figure 2.11, shows that the Imperial Valley/Salton Sea region containing the Brawley fault segments has undergone the most loading from the Coronado Bank sequence. The signal at the northern end of the San Andreas fault is due to the steady-state loading of the system. As the simulation evolves, the previous years' seismic activity culminates in the model year 155450 with a rupture in the south east end of the SAF system similar to the Brawley 1940 event (Figure 2.12).

2.7 CONCLUSIONS

The calculation of the spatial evolution of the gravity signal over a large fault network with complex geometry may act as a proxy for the strain accumulation at depth. Moreover, as gravity is an observable variable in the field, it is a likely candidate for field campaigns or

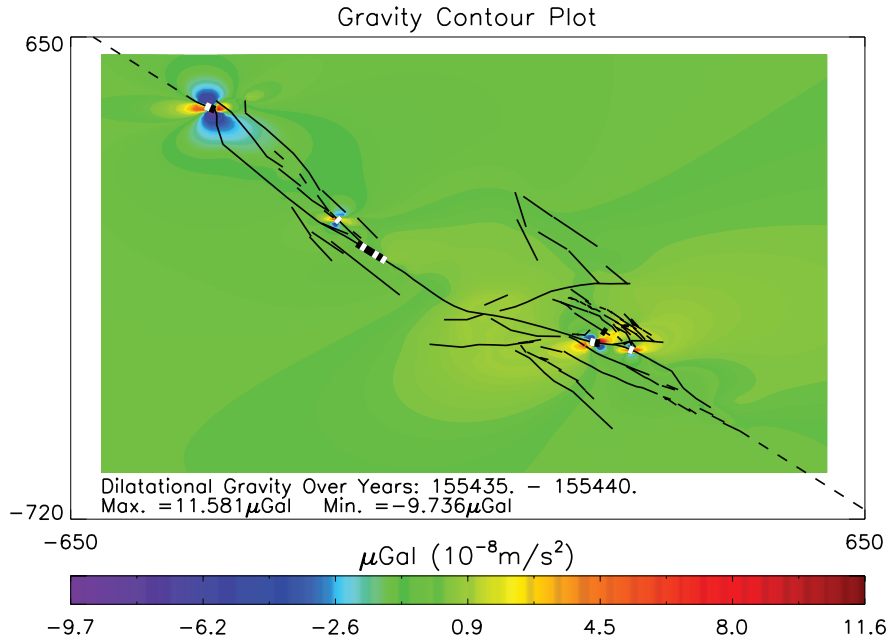


FIGURE 2.9: Five years of the accumulated dilatational gravity for Brawley ending ten years prior to the event.

permanent station deployment using traditional instruments. Here we developed a method for calculating the gravity changes over the fault network and event recurrence scales for California.

Using the Virtual California time dependent stress-evolution earthquake simulation to model slip histories for California, we calculated the gravity evolution over a geometrically complex fault network using the gravity Green's function solutions of *Okubo* (1991, 1992). The method is general enough that the inclusion of dip-slip, tensile motion, and cavity filling matter contributions to gravity can be easily made.

We found that the steady-state component of the gravity signal is within the observable range of current portable instruments when taken over a five year period. More precise instruments, such as a

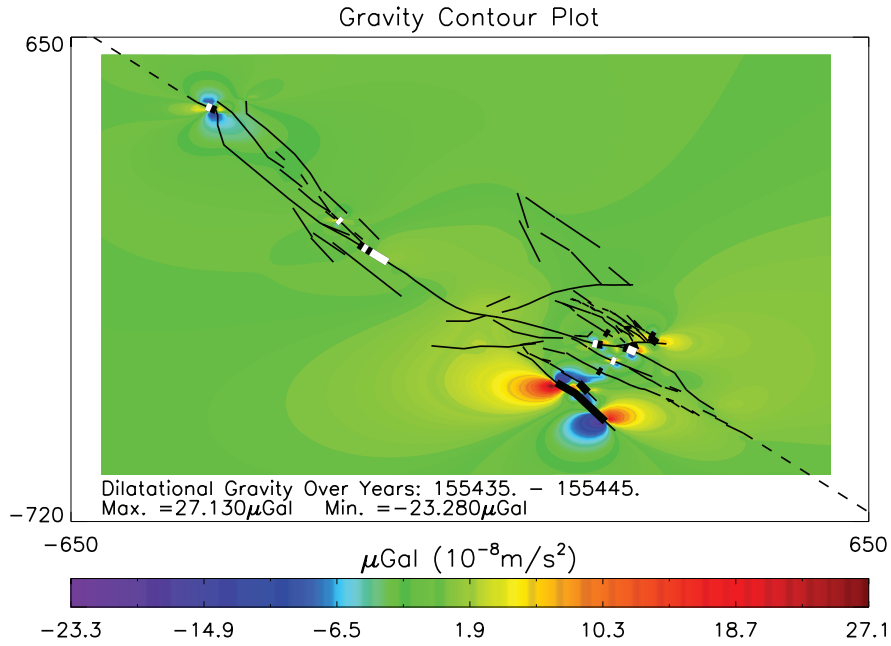


FIGURE 2.10: Ten years of the accumulated dilatational gravity for Brawley ending five years prior to the event.

superconducting gravimeter should be able to readily detect the annual component of the steady-state signal. When moderate sized events occur, the gravity signal generated over large spatial areas is within field instrumentation capabilities, and well within permanent station devices such as SGs or absolute gravimeters.

The presented work demonstrates that the temporal evolution of the gravity signal for strike-slip systems is also a viable candidate for field observations. Ideally, the collection of gravity data would complement the extensive pre-existing GPS and seismic network in California. Permanent gravimeter sites could occupy regions of seismic interest that display persistent, measurable gravity signals in realistic fault models. Anomalous gravity signals can help identify regions of potential seismic risk and aid researchers narrow the focus of their

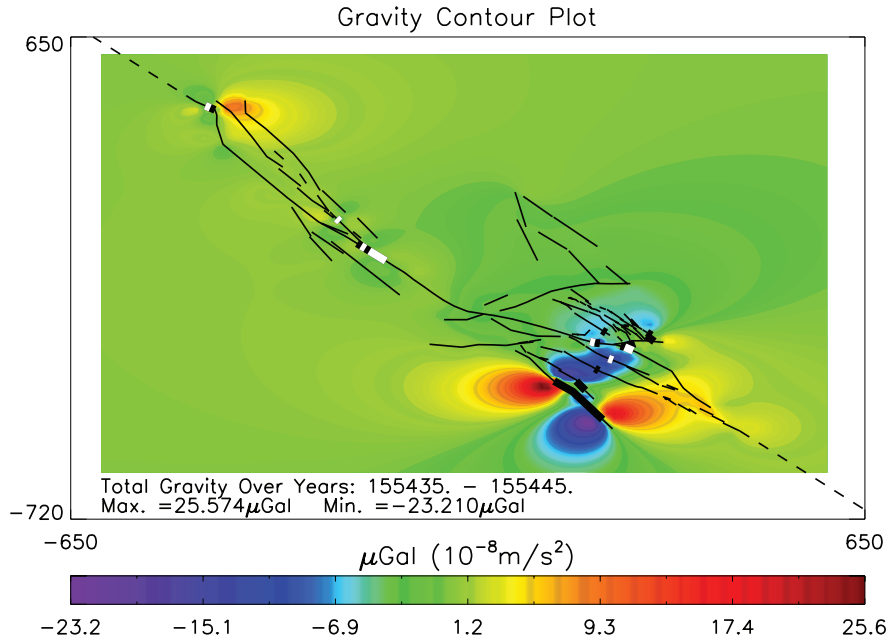


FIGURE 2.II: Ten years of the accumulated total gravity for Brawley ending five years prior to the event (cf. Figure 2.IO.).

observational efforts.

Furthermore, the results of this study suggest that the SAF system is a likely candidate for periodic field campaigns of gravity data collection to specifically obtain accurate pre- and post-seismic gravity maps. Such data can potentially be assimilated into the model to further constrain the frictional parameters and, in turn, the failure recurrence intervals for each fault segment. Moreover, data collected from a large-scale field campaign can be inverse modelled to generate a more realistic picture of the current state of the subsurface stress field and can help provide forecasters with an accurate depiction of the evolution of subsurface stress; highlighting regions with anomalous signals and potentially increased future seismic risk.

We stress that the method presented here is meant to demonstrate

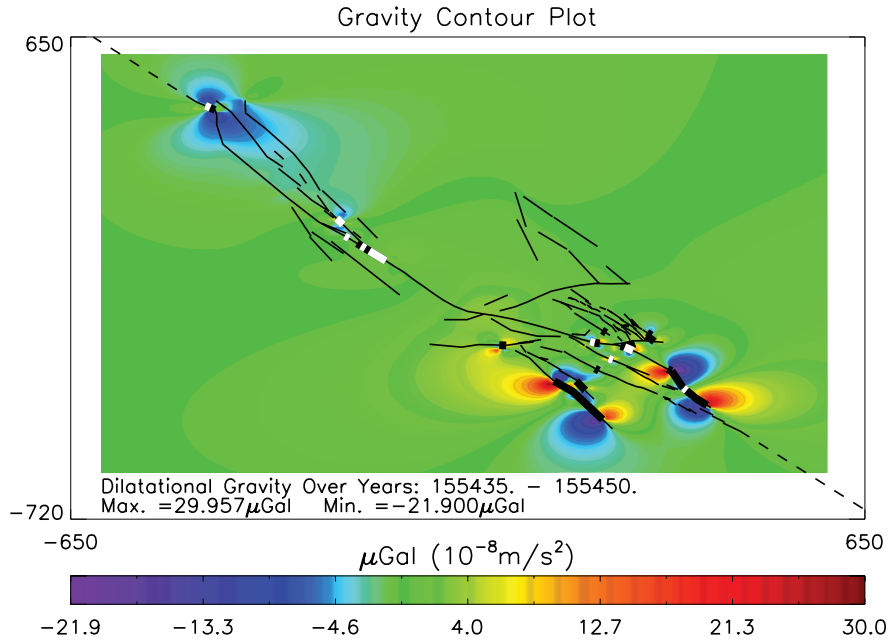


FIGURE 2.12: Fifteen years of the accumulated dilatational gravity for Brawley ending with the rupture in 155450.

that gravity signals for strike-slip systems can complement the existing suite of observational techniques available to researchers. When comparing the model here with collected data, care must be taken to remove other sources of noise in the gravity signal, in particular removal of the free-air gravity signal. The free-air gravity signal is dependent upon height changes from deformation arising from groundwater and other processes which deform the surface. InSAR and GPS data will be of critical assistance in confirming the associated deformation and improving these models via advanced data assimilation techniques (Samsonov and Tiampo, 2006).

Further studies into the behaviour of the spatial evolution of the gravity signals prior to, during, and following, moderate to large events are warranted based on the results presented here. Future work

will include the incorporation of arbitrary dip fault geometries. We also will investigate the possibility of improving the method to include a viscoelastic half-space beneath an overlying elastic half-space (based on *Soldati et al.* (1998)) to more accurately model the free-air signal in the post-seismic regime.

REFERENCES

- Brown, R. D., Jr., *The San Andreas fault system, California*, chap. 4. Quaternary deformation, pp. 83–113, U.S. Government Printing Office, 1990.
- Chinnery, M. A., The deformation of the ground around surface faults, *Bull. Seis. Soc. Amer.*, 51(3), 355–372, 1961.
- Chinnery, M. A., The stress changes that accompany strike-slip faulting, *Bull. Seis. Soc. Amer.*, 53(5), 921–932, 1963.
- Deng, J., and L. R. Sykes, Evolution of the stress field in southern California and triggering of moderate-size earthquakes: A two hundred year perspective, *J. Geophys. Res.*, 102(B5), 9859–9886, 1997.
- King, G. C. P., R. S. Stein, and J. Lin, Static stress changes and the triggering of earthquakes, *Bull. Seis. Soc. Amer.*, 84(3), 935–953, 1994.
- Mansinha, L., and D. E. Smylie, The displacement fields of inclined faults, *Bull. Seis. Soc. Am.*, 61(5), 1433–1440, 1971.
- Maruyama, T., Statical elastic dislocations in an infinite and semi-infinite medium, *Bull. Earth. Res. Inst.*, 42, 289–368, Ph.D. thesis, 1964.
- Massonnet, D., M. Rossi, C. Carmona, F. Adragna, G. Peltzer, K. Feigl, and T. Rabaute, The displacement field of the Landers earthquake

mapped by radar interferometry, *Nature*, 364(6433), 138–142, doi:10.1038/364138a0, 1993.

Okada, Y., Surface deformation due to shear and tensile faults in a half-space, *Bull. Seis. Soc. Amer.*, 75(4), 1135–1154, 1985.

Okada, Y., Internal deformation due to shear and tensile faults in a half-space, *Bull. Seis. Soc. Amer.*, 82(2), 1018–1040, 1992.

Okubo, S., Potential and gravity changes raised by point dislocations, *Geophys. J. Int.*, 105, 573–586, 1991.

Okubo, S., Gravity and potential changes due to shear and tensile faults in a half space, *J. Geophys. Res.*, 97(B5), 7137–7144, 1992.

Press, F., Displacements, strains, and tilts at teleseismic distances, *J. Geophys. Res.*, 70(10), 2395–2412, 1965.

Rundle, J. B., A physical model for earthquakes 1. Fluctuations and Interactions, *J. Geophys. Res.*, 93(B6), 6237–6254, 1988a.

Rundle, J. B., A physical model for earthquakes 2. Application to Southern California, *J. Geophys. Res.*, 93(B6), 6255–6274, 1988b.

Rundle, J. B., and D. D. Jackson, A three-dimensional viscoelastic model of a strike slip fault, *Geophys. J. R. Astro. Soc.*, 49, 575–591, 1977.

Rundle, J. B., and H. Kanamori, Application of an inhomogeneous stress (patch) model to complex subduction zone earthquakes: A discrete interaction matrix approach, *J. Geophys. Res.*, 92(B3), 2606–2616, 1987.

Rundle, J. B., W. Klein, K. Tiampo, and S. Gross, Linear pattern dynamics in nonlinear threshold systems, *Phys. Rev. E*, 61(3), 2418–2431, 2001.

- Rundle, J. B., P. B. R. W. Klein, J. de sa Martins, K. T. A. Donnellan, and L. H. Kellogg, Gem plate boundary simulations for the Plate Boundary Observatory: A program for understanding the physics of earthquakes on complex fault networks via observations, theory, and numerical simulation, *Pure Appl. Geophys.*, 159, 2357–2381, 2002.
- Rundle, J. B., P. B. Rundle, A. Donnellan, and G. Fox, Gutenberg-Richter statistics in topologically realistic system-level earthquake stress-evolution simulations, *Earth Planets Space*, 56, 761–771, 2004.
- Rundle, P. B., J. B. Rundle, K. F. Tiampo, J. S. S. Martins, S. McGinnis, and W. Klein, Triggering dynamics on earthquake fault networks, in *Proc. 3rd Conf. on Tectonic Problems of the San Andreas Fault system*, edited by G. Bokelmann and R. L. Kovach, Stanford U. Publ. Geol. Sci., 2000.
- Samsonov, S., and K. Tiampo, Analytical optimization of a DInSAR and GPS dataset for derivation of three-dimensional surface motion, *IEEE Geoscience and Remote Sensing Letters*, 3(1), 107–111, 2006.
- Smith, B., and D. Sandwell, Coulomb stress accumulation along the San Andreas Fault system, *J. Geophys. Res.*, 108(B6), 2296, doi:10.1029/2002JB002136, 2003.
- Smith, B., and D. Sandwell, A three-dimensional semianalytic viscoelastic model for time-dependent analyses of the earthquake cycle, *J. Geophys. Res.*, 109, B12401, doi:10.1029/2004JB003185, 2004.
- Smith, B. R., and D. T. Sandwell, A model of the earthquake cycle along the San Andreas Fault System for the past 1000 years, *J. Geophys. Res.*, 111(B01405), 1–20, doi:10.1029/2005JB003703, 2006.

- Soldati, G., A. Piersanti, and E. Boschi, Global postseismic gravity changes of a viscoelastic Earth, *J. Geophys. Res.*, 103(B12), 29,867–29,885, 1998.
- Song, T.-R. A., and M. Simons, Large trench-parallel gravity variations predict seismogenic behavior in subduction zones, *Science*, 301, 630–633, 2003.
- Stein, R. S., G. C. P. King, and J. Lin, Stress triggering of the 1994 $m = 6.7$ Northridge, California, earthquake by its predecessors, *Science*, 265, 1432–1435, 1994.
- Steketee, J. A., On Volterra's dislocations in a semi-infinite elastic medium, *Can. J. Phys.*, 36, 192–205, 1958a.
- Steketee, J. A., Some geophysical applications of the elasticity theory of dislocations, *Can. J. Phys.*, 36, 1168–1198, 1958b.
- Sun, W., and S. Okubo, Coseismic deformations detectable by satellite gravity missions: A case study of Alaska (1964, 2002) and Hokkaido (2003) earthquakes in the spectral domain, *J. Geophys. Res.*, 109(B4), B04405, doi:10.1029/2003JB002554, 2004.
- Tiampo, K. F., J. B. Rundle, S. A. McGinnis, and W. Klein, Pattern dynamics and forecast methods in seismically active regions, *Pure Appl. Geophys.*, 159(10), 2429–2467, 2002.
- Tullis, T. E., Rock friction and its implications for earthquake prediction examined via models of Parkfield earthquakes, *Proc. Natl. Acad. Sci. USA*, 93, 3803–3810, colloquim paper, 1996.
- Ward, S. N., San Francisco Bay Area earthquake simulations: A step toward a standard physical model, *Bull. Seis. Soc. Amer.*, 90(2), 370–386, 2000.

Weisbuch, G., *Complex Systems Dynamics: An introduction to automata networks*, Santa Fe Institute Studies in the Sciences of Complexity, vol. 2, Addison-Wesley Publishing Co., 1991.

CHAPTER 3

INVESTIGATING THE ROLE OF DILATATIONAL GRAVITY IN EARTHQUAKE NUCLEATION

Statistics can be made to prove anything – even the truth.

Anonymous

3.1 INTRODUCTION

OMPARISONS of gravity with the subsurface structure have a wide range of applications, traditionally for mineral exploration campaigns. Gravity data has wide appeal in the exploration community as it can be obtained over large spatial scales with high precision and is intuitively interpreted. By comparison, employing gravity for seismic hazard analysis is currently not practised. Despite this, early investigations by *Jachens et al.* (1983) found strong correlations amongst gravity, strain, and elevation data and they further suggested developing a regional gravity monitoring network to act as a proxy for subsurface strain accumulation. To date, however, neither models of gravity accumulation for complex fault networks nor the necessary resolution by instruments exist, thus inhibiting the practical application of gravity monitoring to seismic hazard studies.

[§]Submitted to *Geophysical Research Letters*.

Solutions for gravity changes arising from single-plane thrust-faults and dilatational point sources were first solved for by *Rundle* (1978) and *Walsh and Rice* (1979) respectively. Later, *Okubo* (1991, 1992) developed the general solutions for a single fault plane with arbitrary orientation and slip buried in an elastic half-space. The application of *Okubo* (1992) to complex fault networks that evolve over time, such as California, was developed by *Hayes et al.* (2006) where it was demonstrated that the magnitude of the resultant gravity signal is in the range of current portable instrumentation. Improvements in the technology used to collect gravity data are now sensitive enough to observe changes in crustal dilatation from great earthquakes by the Gravity Recovery and Climate Experiment (GRACE) satellites (*Han et al.*, 2006), and permanent Superconducting Gravimeters have nGal resolution.

We propose that the cumulative dilatational gravity signal over time provides information of the subsurface stress and strain accumulation in complex faults networks. Moreover, that the fault geometry, with respect to the tectonic plate motion that loads the system, plays a key role in determining the likelihood for subsequent triggering of events, and this can be identified in the dilatational gravity signal. The physical interpretation of this signal is consistent with the Coulomb failure criterion. In Section 3.2, we present the our method of analysis of the dilatational signal using the slip histories generated by Virtual California (*Rundle*, 1988a,b); in Section 3.3 we provide the statistical data generated from this analysis; and in Section 3.4, we discuss our results as they pertain to seismic hazard analysis and stress triggering.

3.2 METHOD

3.2.1 GENERATING THE SLIP HISTORIES USING VIRTUAL CALIFORNIA

In order to collect the necessary historical data for our analysis, we must rely on numerical simulations to generate the slip histories. Virtual California (VC), a stress-evolution model, was designed to simulate thousands of years of realistic seismic slip histories for California *Rundle et al.* (2004). Gravity data campaigns by comparison must be collected over large temporal and spatial scales in order to perform a complete statistical analysis, and thus are impractical for our purposes. Nor do we, as yet, have available time series of sufficient length for this purpose. As such, numerical models such as VC are the only means by which one can investigate the statistical behaviour of complex fault systems over various temporal and spatial scales.

In VC, an underlying driver plate loads the fault network at each time step in the simulation. The resultant increase in stress at each of the 650 fault segments is calculated and the fault segment accrues this stress proportionally as back-slip, modulated by a component of stable aseismic slip (stress release) as observed in experiments (*Karner and Marone*, 2000). The process continues until any one segment in the model reaches a pre-defined stress value for failure derived from known recurrence intervals and earthquake magnitudes *Rundle et al.* (2000). The accrued back-slip on that segment is released, and in a series of parallel Monte Carlo sweeps (MCS), VC determines if any other fault segments have reached failure during that time step as a result of the new distribution of stress. This allows for a diverse range of slip histories to be generated, from smaller events like the Joshua Tree earthquake, to large events such as the Fort Tejon earthquake of 1857. This process can be repeated over thousands of years of realizations. Over multiple calculations, VC generates the times, locations, and magnitudes of slip for each of the fault segments, amongst other

variables. It is these slip histories generated by VC that we employ for our study, which were collected for 55 000 years.

3.2.2 CALCULATION OF THE DILATATIONAL GRAVITY OVER 55 000 YEARS

Once the slip histories have been generated, we are in a position to calculate the dilatational gravity values for various time intervals. Using the gravity Green's functions developed by *Okubo* (1992), we calculate the unit slip response for each of the fault segments in the system. The method applies the single fault solutions of *Okubo* (1992) for the entire network and is described in detail by *Hayes et al.* (2006); here we describe the adaptation of that method for our statistical analysis.

Using the time differencing method as outlined by *Hayes et al.* (2006), we calculate the dilatational gravity for time intervals of 2, 12, 15, 20, 50, and 100 years. For each time interval, we calculate the dilatational gravity at the centre of each of the fault segments used in VC. The dilatational gravity is chosen as it quantifies the subsurface density changes from the historical seismicity, i.e., the Bouguer gravity anomaly, and provides a direct method to interpret the results physically. We note that, by convention, regions of *positive* dilatational gravity correspond to regions where the subsurface density has increased due to *compression* arising from the seismic slip and, conversely, regions of *negative* dilatational gravity correspond to an *extensional* regime in the subsurface.

3.2.3 FILTERING OUT THE LONG-TERM TREND FROM THE STEADY-STATE LOADING

Before we can collect the necessary statistics, we need to process the gravity data for each calculation of the time-differenced gravity values.

As the steady-state rates employed in this study are static, the resultant steady-state gravity trend can mask the gravity signals generated by purely elastic seismic slip. For our investigation, we are interested in examining the correlation of the dilatational gravity and the triggering of earthquakes by unstable seismic activity, rather than the long term loading. While the steady-state loading of the system plays a crucial role in generating the slip histories from VC, it produces a two-dimensional spatial trend in the gravity data that acts as noise in our analysis. By artificially suppressing the steady-state gravity Green's functions (calculated separately from the unstable, elastic slip, gravity Green's functions), we were able to remove this unwanted effect.

3.2.4 COLLECTION OF THE GRAVITY STATISTICS

We chose to employ the following methodology to collect our statistics. If a fault segment slipped in the year following the last year of the time differencing calculation and it had a positive dilatational gravity value, we added 1 to the count variable Δg_i^{S+} ; otherwise it remained the same. We note that the superscript, $S+$, indicates positive dilatational gravity *and* slip in the following year, and the subscript, i , indicates the fault segment (i.e., $i = 1 \dots 650$). We also kept track of how many times each fault segment slipped over the entire 55 000 years, regardless of the gravity value, and stored that value in the variable S_i^Σ , i.e., the total number of slip events each fault segment experienced over the course of the simulation.

For example, using a 12 year time interval for our gravity difference calculation, we calculate the dilatational cumulative gravity over the years 0 and 12, including all seismic events during that time interval. If the fault slipped in year 13, and had a cumulative positive dilatational gravity value ending in year 12, we added 1 to Δg_i^{S+} . We then advance

the time step for the time interval by 1 year, and repeat the same process for years 1 to 13, and determine whether or not slip occurred in year 14, for each segment. This was done for the entire slip history generated by VC in a 55,000 year simulation. Conceptually, one can think of this method as being analogous to collecting gravity data in a field campaign, and returning to collect data once again in 2, 12, 15, 20, 50, and 100 years, and comparing those changes in the system from the initial campaign. At the end of sliding the time differencing calculation along in this manner, we found the percentage of times that a fault segment had a positive dilatational gravity value prior to slip by calculating the ratio,

$$P_i^{\Delta g} = \frac{\Delta g_i^{S+}}{S_i^{\Sigma}} \quad (3.1)$$

3.3 RESULTS

For our analysis, we collected data for each fault segment in the VC simulator, but we present here the results for four regions as identified in Figure 3.3. In Figures 3.3 and 3.3, we plot the value $P_i^{\Delta g}$ for each of the regions highlighted in Figure 3.3. We note that for the San Andreas, Northern San Andreas, and Big Bend sections, the fault segment numbers increase from north to south along the San Andreas. For the Mojave section, the values are plotted in the fault numbering sequence assigned in the data assimilation process for VC and, in general, the individual faults are plotted from north to south, traversing west to east.

Spatial analysis of the positive dilatational signal over the time histories is achieved via map plots of the data in Figures 3.3 and 3.3. In Figure ?? we plot $P_i^{\Delta g}$ for the entire model for the 20 year time interval alongside a zoomed image of the Big Bend region. A

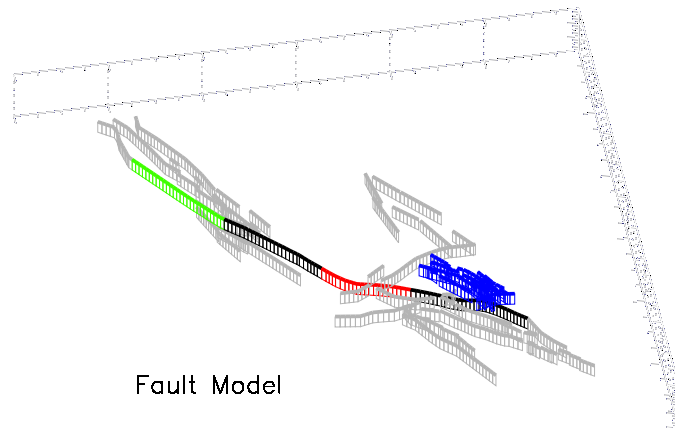


FIGURE 3.1: Fault segments used in the VC simulator. The San Andreas section used in the analysis is comprised of the black, green, and red segments. The green segments are the Northern San Andreas, the red segments are the ‘Big Bend’ region, and the blue segments are the Mojave fault segments.

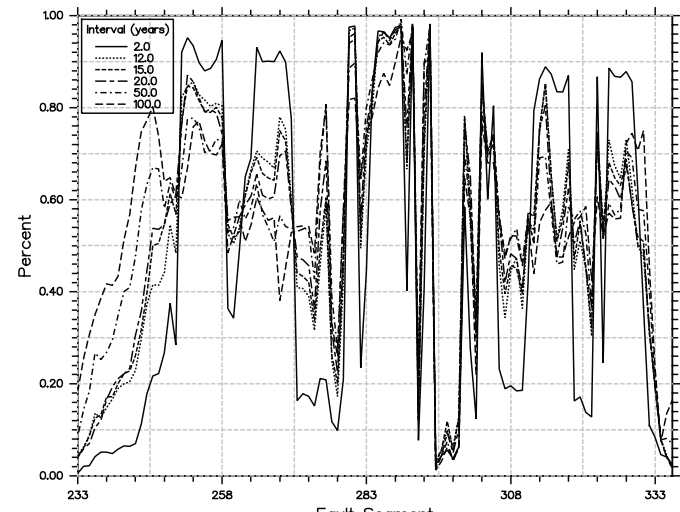
similar plot for the Northern San Andreas regions, Figure 3.3, is given using a 12 year interval for our analysis. The advantage of using the map plots is that it allows one to correlate the cool colours with the physical interpretation that the section predominantly slips when the dilatational gravity is extensional and, similarly, the warm colours indicate slip occurred predominantly when the dilatational gravity was compressional.

3.4 DISCUSSION

In order to interpret the results from the data, we must recall that the long-term loading signal has been removed. As such, these results represent how the regional seismic activity acts to amplify or dampen

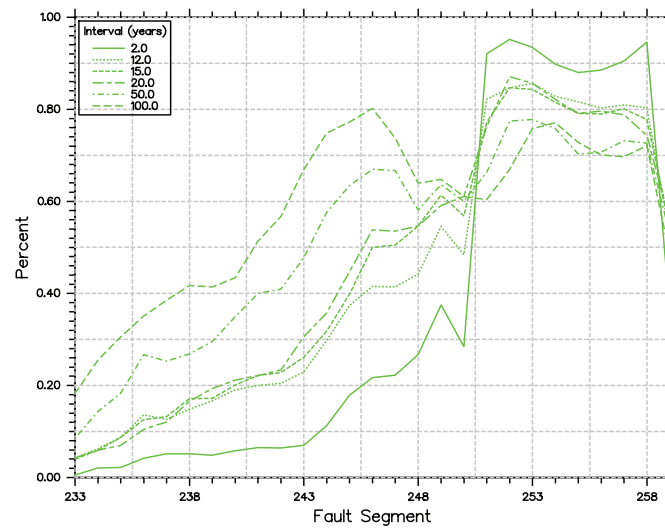
8

Positive gravity values by region
San Andreas



(a)

Positive gravity values by region
Northern SA



(b)

FIGURE 3.2: The values of $P_i^{\Delta g}$ for time interval are plotted against the fault segments indicated in Figure 3.3 for (a), the San Andreas fault and, (b), the Northern San Andreas.

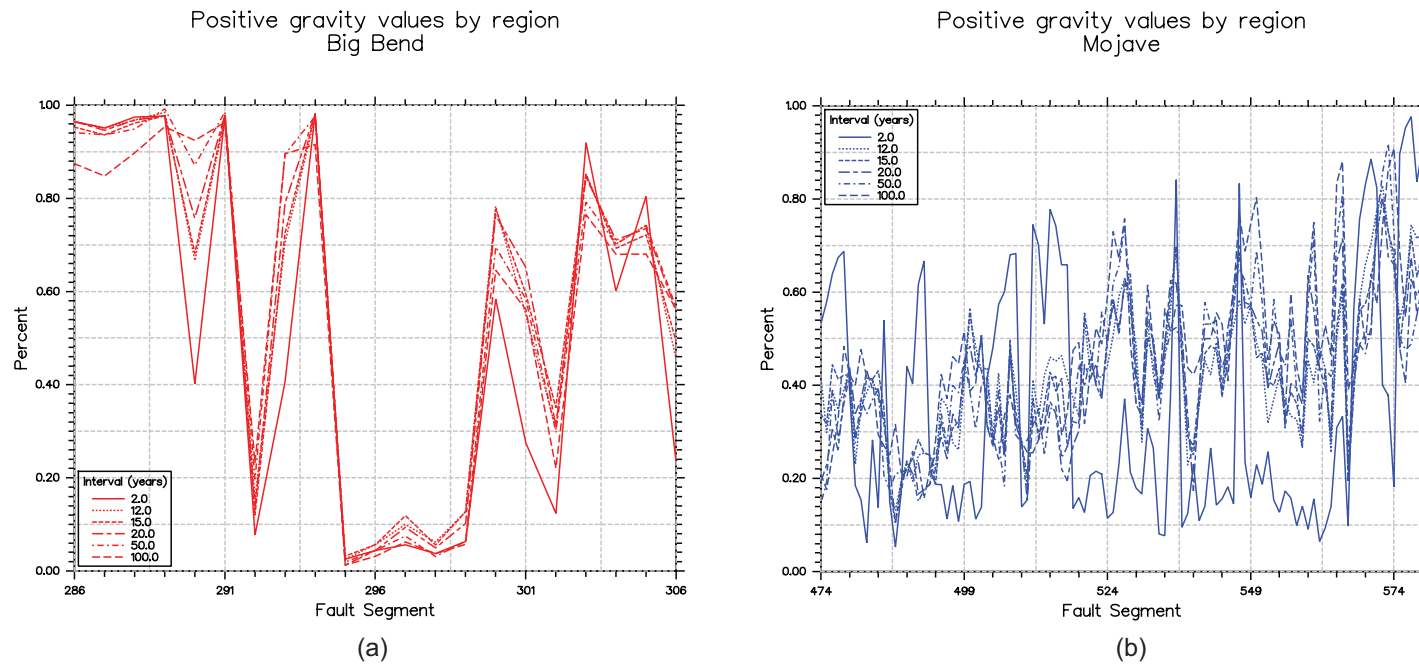


FIGURE 3.3: The values of $P_i^{\Delta g}$ for time interval are plotted against the fault segments indicated in Figure 3.3 for (a), the Big Bend section and, (b), the Mojave faults.

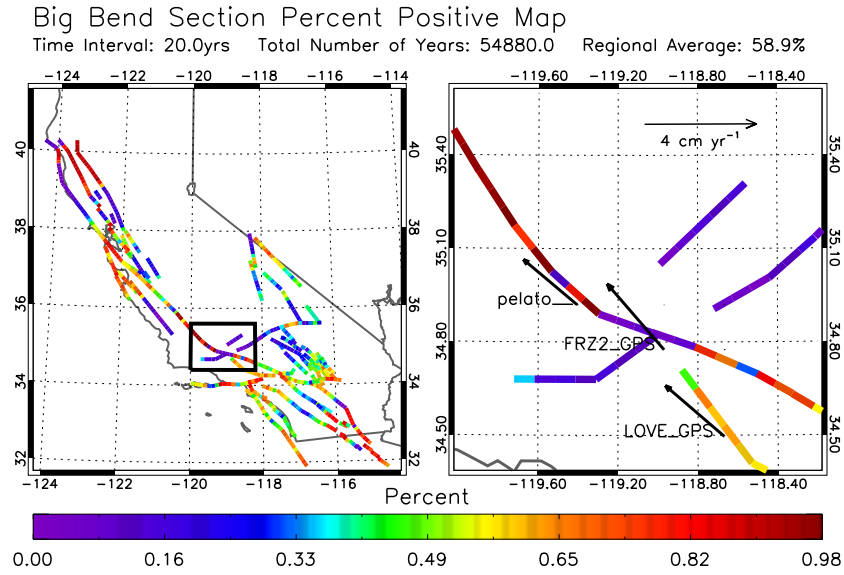


FIGURE 3.4: Plot of $P_i^{\Delta g}$ for the 20 year time interval. Total number of years used in the creation of the map is indicated at the top of the figure, along with the regional average of positive dilatational gravity preceding slip for the segments in red in Figure 3.3. In the zoomed Big Bend region, indicated by the black square, we have also plotted GPS velocities referenced to a fixed North American plate *Shen et al.* (1998).

the steady-state stress in the system. That is, these plots help interpret how stress changes induced by particular sequences of earthquakes can act to trigger subsequent events on neighbouring fault segments.

The map view plot of the Big Bend region (Figure 3.3), exhibits strong correlation with predominantly positive dilatational gravity signals on fault segments whose orientation is strongly parallel with the plate velocity. Conversely, where the Big Bend is oriented in a more oblique fashion, the predominant mechanism prior to slip is un-clamping of the fault, as suggested by the low percentages of posi-

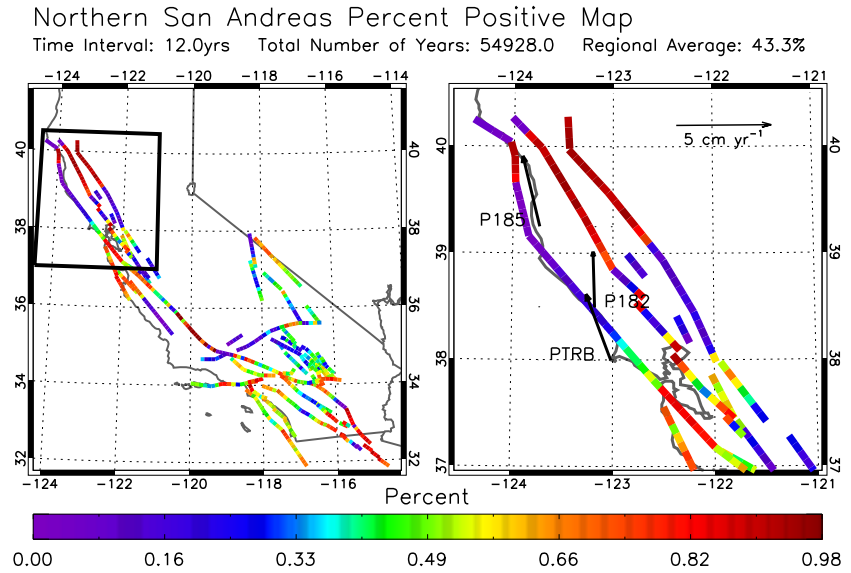


FIGURE 3.5: Plot of $P_i^{\Delta g}$ for the 12 year time interval. Total number of years used in the creation of the map is indicated at the top of the figure, along with the regional average of positive dilatational gravity preceding slip for the segments in red in Figure 3.3. In the zoomed Northern San Andreas region, indicated by the black square, we have also plotted GPS velocities referenced to a fixed North American plate USGS (2007).

tive dilatational gravity. We interpret this observation in terms of the Coulomb failure criterion, i.e.,

$$\sigma^F = \sigma_{xy} - \mu \sigma_{xx} \quad (3.2)$$

Here σ^F is the condition for failure, σ_{xy} is the shear stress, μ is the coefficient of internal friction, σ_{xx} is the normal component of stress, and failure on a fault is more likely to occur when the value σ^F increases above the existing fault strength *King et al.* (1994).

Low percentages of positive dilatational gravity suggests that trig-

gering of an earthquake in that region, the normal component of stress, σ_{xx} , on the fault is reduced preferentially. This value of σ_{xx} is reduced in punctuated intervals by seismic activity. The cumulative effect acts to increase σ^F in (3.2), eventually resulting in enough of a reduction to overcome the long-term loading, progressive un-clamping of the fault, and subsequent failure. Further, the orientation of the fault with respect to the plate motion at these predominantly low percentage sites seems to indicate that σ_{xx} is the primary control on whether or not slip occurs when the fault is oriented obliquely to the direction of plate motion. That is to say, the precursory dilatational gravity signal tends to be dominated by an extensional regime. We note that this tendency occurs for each time interval as shown in Figure 3.3.

In those regions where the predominantly positive dilatational gravity signal is present, the interpretation is that the region is now aligned with the long-term loading direction. Where predominantly constant compressional loading, acting to increase σ_{xy} , is the primary mechanism for failure. We suggest that the forces imparted by seismic events in these regions tend to increase both σ_{xx} and σ_{xy} , but the change in σ_{xy} contributes in such a way so as to further amplify the shear stress imparted by the long-term loading. By continuing to preferentially increase σ_{xy} , the net result over time is to increase σ^F , and thus the likelihood of failure. Indeed, even the San Gabriel fault zone, just south of the Big Bend and parallel to the San Andreas, exhibits the same predominantly positive precursory dilatational gravity signal. As such, this indicates there exists a strong relationship between fault orientation, the long-term stress loading, and the mechanisms responsible for triggering subsequent earthquakes.

In the Northern San Andreas section, we observe the same high percentages for positive dilatational gravity at the southern end of the

zoomed region. However, the northern section exhibits more complicated behaviour. We note that the dynamics driving the system are affected by the locked portion of the Cascadia Subduction Zone (CSZ) to the north. This imparts a significant component of contraction in the direction of the CSZ's motion *Williams et al.* (2006). Moreover, the suite of parallel faults to the east of the San Andreas may be affecting how the strain arising from seismic activity is distributed along the San Andreas. As such, the complicated geometry of the region, and its diverse components of long-term loading, affect the system in a more complicated manner than the Big Bend.

Examination of the entire map view of the percentage data for the Mojave faults (shown on the left-hand side of Figure 3.3) clearly shows that the values for a dominantly positive dilatational signal increase towards the southern portion of the region. The apparent sinusoidal structure, shown in Figure 3.3(b) is due to the fault numbering associated with that region. Despite the apparent trend of predominantly positive dilatational gravity in the south, to predominantly negative dilatational gravity in the north, caution is warranted in analyzing these results. The recurrence intervals in the Mojave are poorly constrained and our current incarnation of VC does not yet incorporate dip-slip faults which may play a significant role in the stress evolution of the entire system.

The results of this preliminary analysis using gravity to interpret the mechanism for seismic nucleation are promising and suggest that it can play an integral role in the analysis and evaluation of earthquake triggering and potential seismic hazard. The magnitude of the long-term, steady-state gravity signal over five years is $\pm \sim 2 \mu\text{Gal}$; the current limit of portable instrument resolution (*Hayes et al.*, 2006). Unstable seismic slip magnitudes for moderate-sized to large-sized events range from $\sim 10 \mu\text{Gal}$ to $\sim 80 \mu\text{Gal}$ (*Hayes et al.*, 2006). This suggests

that a monitoring strategy incorporating both permanent gravimeters and periodic field campaigns would be able to detect these changes over time. Interpretation of the gravity data in our analysis suggests a strong relationship between fault orientation, with respect to the long-term normal stress driving the system, and subsequent triggering of earthquakes. Finally, the unique advantage of gravity data collected at the surface is that gravity contains information integrated over all depths, and inversion methods can serve to further constrain estimates of subsurface processes of stress accumulation. By contrast, all other techniques must infer subsurface stress and strain based on their expression at the surface. Further study of gravity, and its relationship to stress and strain in fault networks, will allow researchers to quantify how gravity may be employed to complement GPS, InSAR, and traditional strain meter data.

REFERENCES

- Han, S.-C., C. K. Shum, M. Bevis, C. Ji, and C.-Y. Kuo, Crustal dilatation observed by GRACE after the 2004 Sumatra-Andaman earthquake, *Science*, 313, 658–662, doi:10.1126/science.1128661, 2006.
- Hayes, T. J., K. F. Tiampo, J. B. Rundle, and J. Fernández, Gravity changes from a stress evolution earthquake simulation of California, *J. Geophys. Res.*, 111, B09,408, doi:10.1029/2005JB004092, 2006.
- Jachens, R. C., W. Thatcher, C. W. Roberts, and R. S. Stein, Correlation of changes in gravity, elevation, and strain and southern California, *Science*, 219, 1215–1217, 1983.
- Karner, S. L., and C. Marone, *GeoComplexity and the Physics of Earthquakes*, *Geophysical Monograph*, vol. 120, chap. Effects of loading rate

and normal stress on stress drop and stick-slip recurrence interval, pp. 187–198, American Geophysical Union, 2000.

King, G. C. P., R. S. Stein, and J. Lin, Static stress changes and the triggering of earthquakes, *Bull. Seis. Soc. Amer.*, 84(3), 935–953, 1994.

Okubo, S., Potential and gravity changes raised by point dislocations, *Geophys. J. Int.*, 105, 573–586, 1991.

Okubo, S., Gravity and potential changes due to shear and tensile faults in a half space, *J. Geophys. Res.*, 97(B5), 7137–7144, 1992.

Rundle, J. B., Gravity changes and the Palmdale uplift, *Geophys. Res. Lett.*, 5(1), 41–44, 1978.

Rundle, J. B., A physical model for earthquakes 1. Fluctuations and Interactions, *J. Geophys. Res.*, 93(B6), 6237–6254, 1988a.

Rundle, J. B., A physical model for earthquakes 2. Application to Southern California, *J. Geophys. Res.*, 93(B6), 6255–6274, 1988b.

Rundle, J. B., P. B. Rundle, A. Donnellan, and G. Fox, Gutenberg-Richter statistics in topologically realistic system-level earthquake stress-evolution simulations, *Earth Planets Space*, 56, 761–771, 2004.

Rundle, P. B., J. B. Rundle, K. F. Tiampo, J. S. S. Martins, S. McGinnis, and W. Klein, Triggering dynamics on earthquake fault networks, in *Proc. 3rd Conf. on Tectonic Problems of the San Andreas Fault system*, edited by G. Bokelmann and R. L. Kovach, Stanford U. Publ. Geol. Sci., 2000.

Shen, Z., L. Sung, D. Dong, B. King, T. Herring, and S. McClusky, Horizontal Deformation Velocity Map: Version 2.0, Online, Crustal Deformation Working Group (SCEC), http://www.data.scec.org/group_e/release.v2/, 1998.

USGS, Earthquake Hazards Program, Online,
<http://quake.wr.usgs.gov/research/deformation/gps/auto/CN.html>,
2007.

Walsh, J. B., and J. R. Rice, Local gravity changes resulting from deformation, *J. Geophys. Res.*, 84(B1), 165–170, 1979.

Williams, T. B., H. M. Kelsey, and J. T. Freymueller, Gps-derived strain in northwestern California: Termination of the San Andreas fault system and convergence of the Sierra NevadaGreat Valley block contribute to southern Cascadia forearc contraction, *Tectonophysics*, 413, 171–184, doi:10.1016/j.tecto.2005.10.047, 2006.

CHAPTER 4

A GRAVITY GRADIENT METHOD FOR CHARACTERIZING THE POST-SEISMIC DEFORMATION FIELD FOR A FINITE FAULT

Discovery consists of seeing what everybody has seen and thinking what nobody has thought.

Albert Szent-Györgyi

4.1 INTRODUCTION



THE ANALYTIC solutions of the deformation field from seismic events are well established in the literature for elastic half-spaces (*Chinnery*, 1963; *Mansinha and Smylie*, 1971; *Okada*, 1985), and further developed for the corresponding stress and strain fields (*Okada*, 1992). Seismic triggering studies that interpret the Coulomb stress changes arising from the resultant deformation field after a seismic event have demonstrated the potential for identifying regions of future seismic activity (*King et al.*, 1994; *Stein et al.*, 1994; *Freed and Lin*, 2001). However, the Coulomb stress changes are inherently unobservable by direct measurement and are typically restricted to surface observations; their values at focal depths must be inferred.

By contrast with stress and strain measurements, gravity observations record changes from all depths and their acquisition over large

[‡]Submitted to *Geophysical Journal International*.

spatial scales is common, due in large part to their extensive use in exploration geophysics. The analytic solutions for the gravity changes from an earthquake were first numerically solved for by *Rundle* (1978), and analytically solved for a thrust fault and dilatational point source by *Walsh and Rice* (1979). *Okubo* (1991, 1992) developed the general solutions for a finite fault within a half-space and further extended for complex fault networks by *Hayes et al.* (2006). *Walsh and Rice* (1979) explicitly derive the dilatational solutions in terms of the stresses induced in the subsurface medium and, as demonstrated by *Okubo* (1992), the dilatational, or Bouguer, gravity anomaly corresponds directly to the subsurface density from seismic activity. Often, of more practical use in exploration geophysics are the gravity gradient, which delineate the edges of subsurface density anomalies (*Bell*, 1997; *Saad*, 2006). As such, it follows that the gravity gradients, may provide more detailed information on the spatial distribution of the deformation field following an earthquake and, in turn, its subsurface stress and strain.

The purpose of this paper is to provide the analytic gravity gradient solutions for a vertical strike-slip finite fault within an elastic half-space. In Section 4.2, we outline our method and solutions. Section 4.3 shows the results for several of the gradient solutions followed by a discussion of the results in Section 4.4.

4.2 THE GRAVITY GRADIENT SOLUTIONS

In order to calculate the gravity gradient changes for an earthquake, we first use the gravity Green's functions developed by *Okubo* (1992). In general, the expressions used for the dilatational gravity changes

are given by:

$$\begin{aligned}\Delta g^*(x_1, x_2) = & \{\rho G[U_1 S_g^*(\xi, \eta) + U_2 D_g^*(\xi, \eta) \\ & + U_3 T_g^*(\xi, \eta)] + \Delta \rho U_3 C_g^*(\xi, \eta)\}\|\end{aligned}\quad (4.1)$$

where ρ is the density of the medium, G is Newton's Universal gravitational constant, ξ and η are coordinates on the fault length and width respectively, U_i is the slip vector. We have used the double vertical notation of Chinnery (1961). For our analysis, we need only focus on the strike-slip component, where $S_g^*(\xi, \eta)$ is given by,

$$\begin{aligned}S_g^*(\xi, \eta) = & (1-2\nu) \tan \delta \{-R - 2\xi I_1 \tan \delta \\ & + q \sec \delta [\sin \delta \cdot \log(R+\eta) - \log(R+d)]\}\end{aligned}\quad (4.2)$$

and note that,

$$I_1(\xi, \eta) = \tan^{-1} \left(\frac{-q \cos \delta + (1+\sin \delta)(R+\eta)}{\xi \cos \delta} \right)\quad (4.3)$$

In expressions (4.1) to (4.3), ν is Poisson's ratio, d is the depth to the bottom of the fault beneath the origin, and $\xi \equiv x_1 - \xi'$, $\eta \equiv p - \eta'$, where,

$$\begin{aligned}p & \equiv x_2 \cos \delta + (d - x_3) \sin \delta \\ R & \equiv \sqrt{\xi^2 + \eta^2 + q^2} \\ q & = x_2 \sin \delta - (d - x_3) \cos \delta \\ d & = \eta \sin \delta - q \cos \delta\end{aligned}$$

See Okubo (1992), Figure 2, for a complete description of the coordinate system used.

In order to calculate the gravity gradients, we first define the operators for the gravity Green's function given by (4.1), which simplify to

the following expressions for a vertical strike-slip fault, i.e., $\cos\delta=0$.

$$\begin{aligned}\frac{d}{dx_1} &= \frac{\partial\xi}{\partial x_1} \frac{\partial}{\partial\xi}|_{x_3=0} \\ \frac{d}{dx_2} &= \frac{\partial q}{\partial x_2} \frac{\partial}{\partial q}|_{x_3=0} \\ \frac{d}{dx_3} &= -\frac{\partial p}{\partial x_3} \frac{\partial}{\partial\eta}|_{x_3=0}\end{aligned}\quad (4.4)$$

In general, the above operators can be used on the gravity potential solutions of *Okubo* (1992) (denoted as P) to find the horizontal gravity solutions as well as their respective gradients for vertical strike-slip systems. Of the nine solutions for the full gravity gradient tensor, five are independent. The independent solutions are: P_{xx} , $P_{xy} = P_{yx}$, $P_{zx} = P_{xz}$, $P_{zy} = P_{yz}$, and P_{zz} , where the subscripts indicate the derivatives and $x = x_1$, $y = x_2$, $z = x_3$ using the coordinate system of *Okubo* (1992). The final dependent solution, P_{yy} can be found using Laplace's equation where, $P_{yy} = -P_{xx} - P_{zz}$ for a closed system (*Walsh and Rice*, 1979).

For the purposes of this paper, we provide the x_1 , x_2 , and x_3 Green's function gravity gradients, i.e., the vertical gravity gradient, $d^2P_g/dx_3^2 = P_{zz}$, and the horizontal gravity gradients given by, $d^2P_g/dx_3dx_1 = P_{zx}$ and $d^2P_g/dx_3dx_2 = P_{zy}$, using (4.1) for a vertical strike-slip fault. For this case, where $\cos\delta=0$, we find the following expressions for the gravity gradient Green's functions.

$$S_{gz}^*(\xi, \eta) = (1-2\nu) \frac{q}{R(R+\eta)} \quad (4.5)$$

$$S_{gx}^*(\xi, \eta) = (1-2\nu) \frac{q\xi}{R(R+\eta)^2} \quad (4.6)$$

$$S_{gy}^*(\xi, \eta) = -(1-2\nu) \left(\frac{1}{R+\eta} - \frac{q^2}{R(R+\eta)^2} \right) \quad (4.7)$$

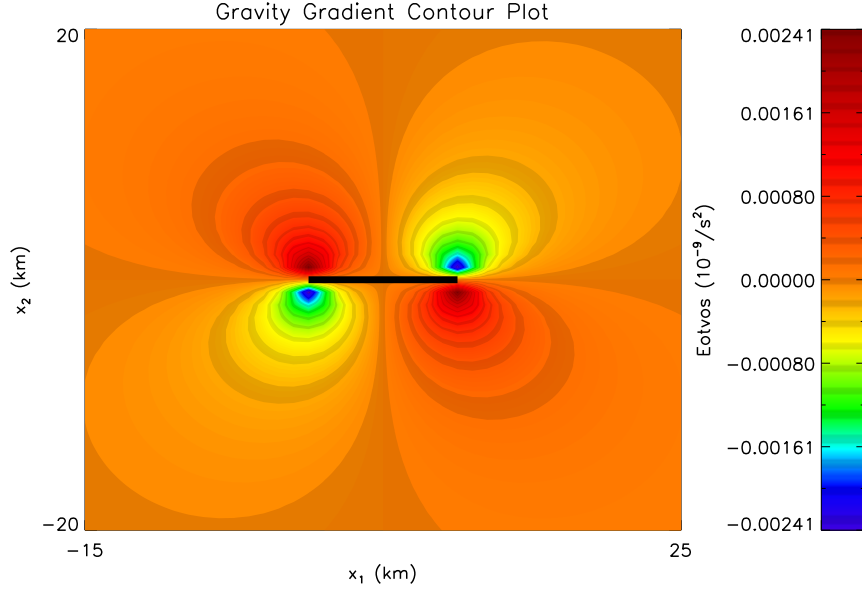


FIGURE 4.1: The vertical gravity gradient for a vertical right-lateral strike-slip fault. $L = 10\text{km}$, $W = 10\text{km}$, depth to the top of the fault is 1km , and the dislocation is 5m . The units are in Eötvös (E), which is equivalent to $0.1\mu\text{Gal}/\text{m}$, or 10^{-9}s^{-2} . The thick black line is the location of the fault.

4.3 RESULTS

Using the Green's functions (4.5) to (4.7) in (4.1), we can calculate the gravity gradient solutions for a vertical strike-slip fault. In Figure 4.1, we plot the vertical gravity gradient using (4.5) for a right-lateral strike-slip fault. The vertical gravity gradient exhibits a similar antisymmetric butterfly pattern as that for the dilatational gravity (See *Okubo, 1992, Figure 4*).

For the horizontal gradients, we make note of the fact that they are coordinate dependent, and thus their derivatives are dependent upon the direction in which their derivatives are found. The consequence of

this is that derivatives in either the positive or the negative direction will produce similar spatial patterns, but with opposite signs. As such, we plot only the magnitude of the horizontal components. We further note that we have employed the use of the more common unit for gravity gradients in exploration geophysics, i.e., the Eötvös (E), where $1E = 0.1 \mu\text{Gal}/\text{m}$, or 10^{-9}s^{-2} in S.I. units.

In Figure 4.2(a) and (b), the solutions to (4.6) and (4.7) are shown respectively. The y -component of the gravity gradient has a larger magnitude than the corresponding x -component of the gravity gradient; however, the pattern produced by the x -component exhibits a more diverse topology and spatially complex signal.

A common technique in exploration geophysics is to examine the various combinations of the gravity gradients in order to further delineate the extent of the subsurface density anomaly. We examine here a linear combination of (4.5), (4.6), and (4.7). In Figure 4.3, we present two cases where we have added the components of the gravity gradient in the following manner.

$$\epsilon P^* - P_{zx} \quad (4.8)$$

Where ϵ is used as a dimensionless scaling factor, from 0 to 1, and $P^* = P_{zz} + P_{zy}$. The scaling factor is used to generate comparable magnitudes of the z - and y -component of the gravity gradient as the smaller x -component values, which would otherwise be masked by these stronger signals.

In Figure 4.3, we demonstrate how the effect of the scaling factor, ϵ , affects the resulting spatial distribution of the signal. As expected, the smaller value of ϵ in Figure 4.3(a), yields a signal with a greater component of the horizontal gravity gradient in the x -direction. This has the effect of retaining the slight negative values in the top-left

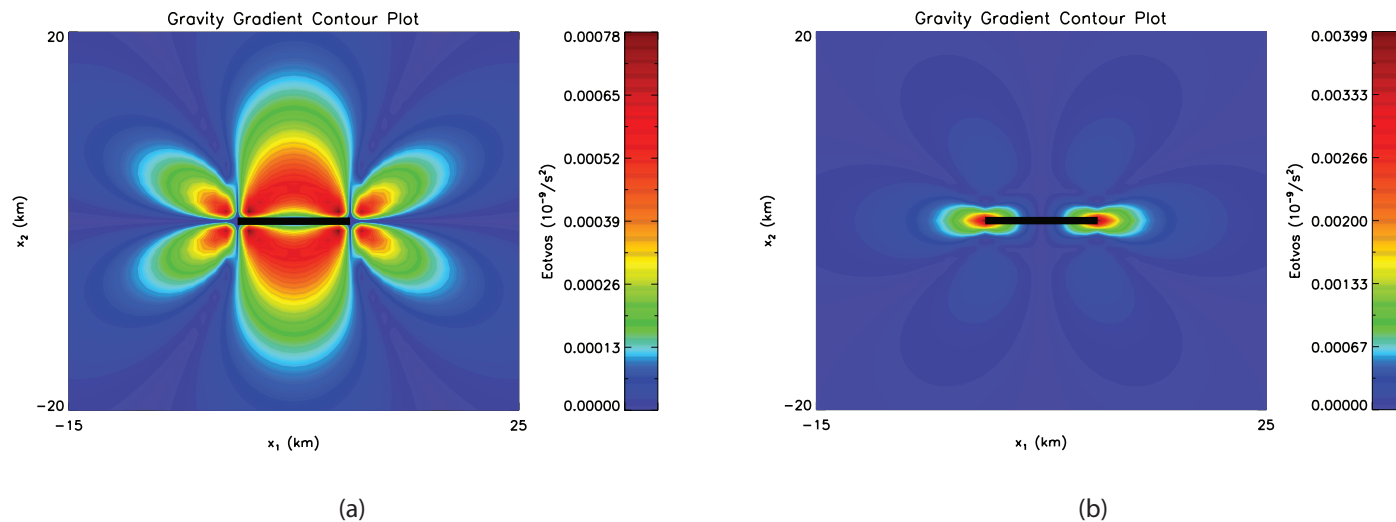


FIGURE 4.2: (a) The x -horizontal gravity gradient magnitude for a vertical right-lateral strike-slip fault, and (b), the y -horizontal gravity gradient magnitude. Parameters used in (a) and (b) are the same as those used in Figure 4.1. *N.B.* that the scales are different in (a) and (b).

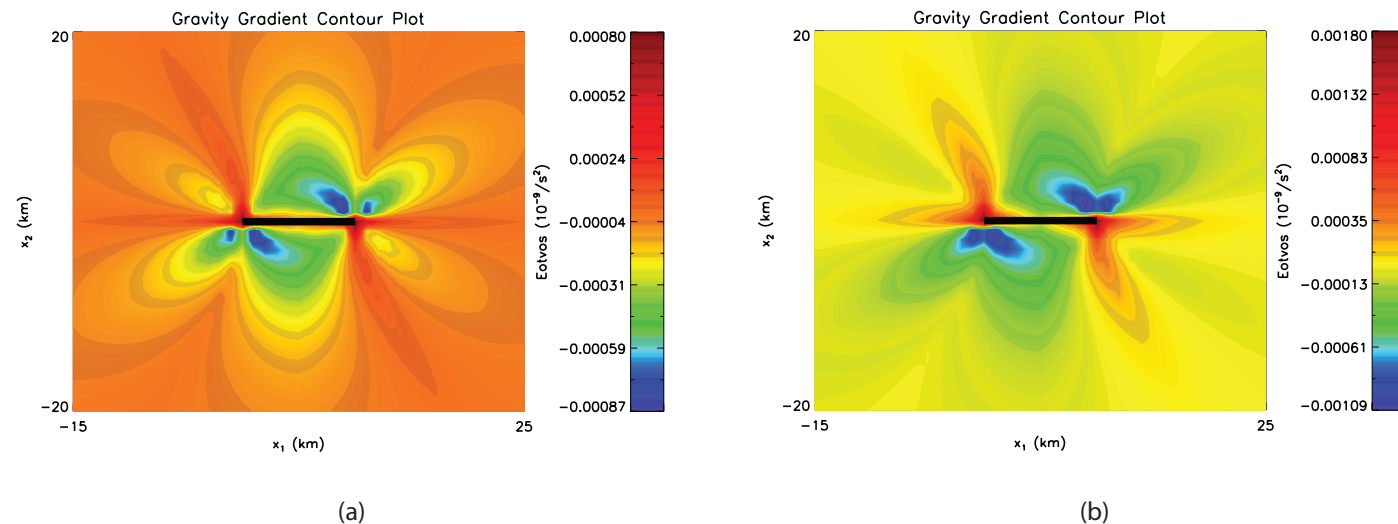


FIGURE 4.3: (a) The gravity gradient solution given by (4.8) with $\epsilon = 0.15$ and (b) $\epsilon = 0.4$. Parameters are the same as those used in Figure 4.1. *N.B.* that the scales are different in (a) and (b).

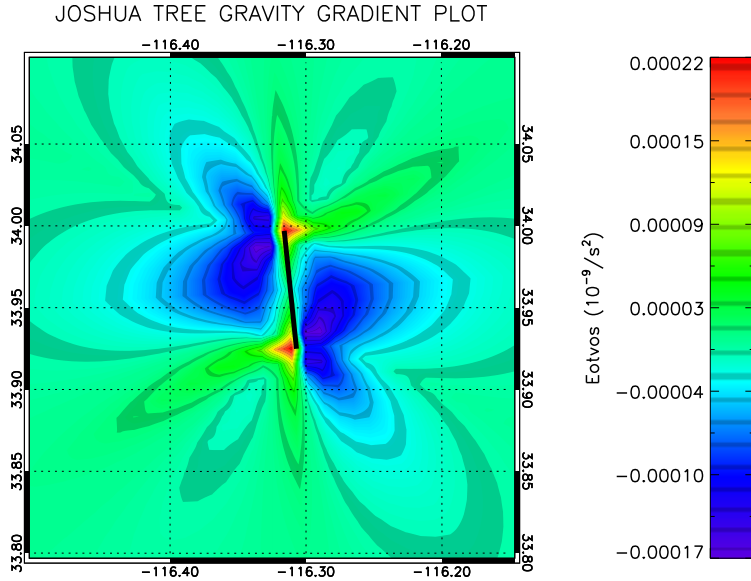


FIGURE 4.4: The gravity gradient solution of (4.8) for the Joshua Tree earthquake of April, 1992. The parameters are $L = 8\text{km}$, $W = 10\text{km}$, with a right-lateral dislocation of 0.8m , and an ϵ value of 0.35 . In order to avoid singularities, the depth to the top of the fault is 500m . The thick black line indicates the approximate location of the Joshua Tree Fault.

and bottom-right quadrants of the signal. The larger ϵ value in Figure 4.3(b) almost masks these signals completely.

Using the source parameters and fault dimensions for the Joshua Tree earthquake, as given by *Bennett et al. (1995)*, we apply the gravity gradient solution in (4.8) with $\epsilon = 0.35$. For comparison purposes, we also provide the Coulomb stress change in Figure 4.5 using the Coulomb 3.0 software (*Lin and Stein, 2004; Toda et al., 2005*). It should be noted that, in order to have a more consistent comparison with Figure 4.4, Figure 4.5 does not include the regional stress component as it is currently not included in the gradient solutions.

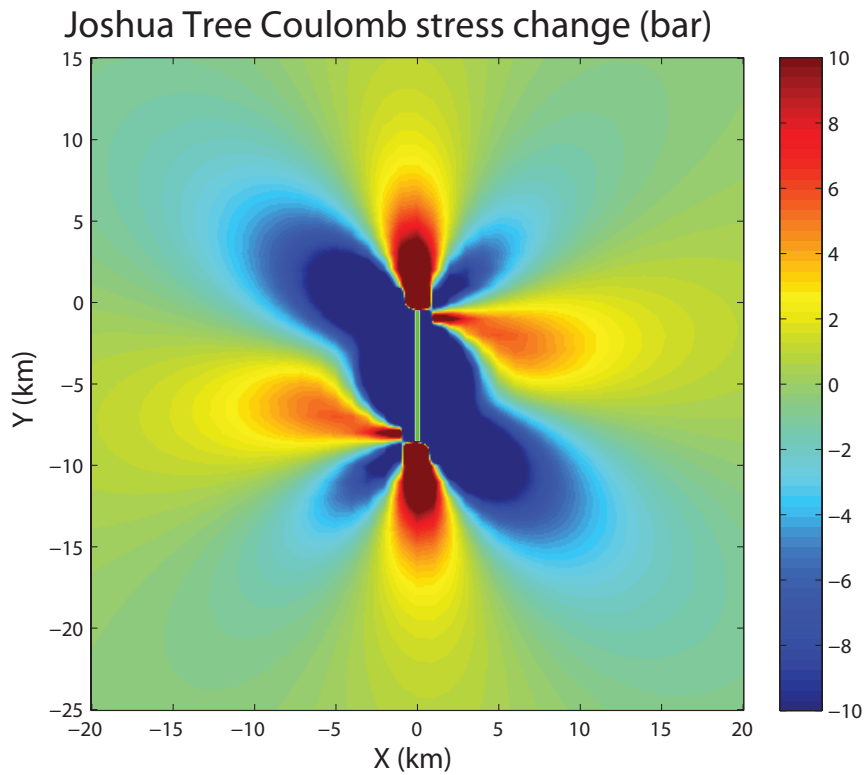


FIGURE 4.5: The Coulomb stress change for the Joshua Tree earthquake of April, 1992. The parameters used are the same as in Figure 4.4, calculated at a depth of 8km, and using a coefficient of friction value of 0.40. The thin green line indicates the approximate location of the Joshua Tree fault.

We observe similarities in the spatial distribution for the gravity gradient plot of Figure 4.4 and the Coulomb stress change plot of Figure 4.5. Moreover, we note that by using (4.4) we solve for the expected gravity gradient solution at the surface, whereas the Coulomb stress changes are calculated at depth.

4.4 DISCUSSION

Using the gravity gradients to delineate the edges of subsurface density anomalies, we have provided the gravity gradient Green's function solutions for the subsurface density anomalies in the post-seismic regime for a vertical strike-slip fault. The physical relationship between the gravity gradients and the corresponding Coulomb stress changes for the deformation field of a finite, strike-slip fault is clearly evident in the similar spatial distributions of Figure 4.3 and Figure 4.4 respectively. Moreover, *Walsh and Rice* (1979) have shown explicitly that the gravity solutions for a dilatational point source and dip-slip fault can be found in terms of the stress changes following seismic events.

As such, the use of gravity gradients may offer researchers the ability to map the actual Coulomb stress changes by using the gradients as a proxy for the stress changes in the system. Furthermore, we suggest this may offer a practical complement to the traditional suite of seismic hazard assessment tools such as combined InSAR and GPS methods (*Samsonov and Tiampo*, 2006); statistical seismicity methods (*Bowman and King*, 2001; *Tiampo et al.*, 2002); in addition to traditional Coulomb stress change solutions (*King et al.*, 1994; *Freed and Lin*, 2001).

Exploration techniques of the 1930's commonly yielded gravity gradient resolutions on the order of magnitude of $\pm 1 \text{ E}$ (*Bell*, 1997), and recent developments in quantum-based instruments promise improved sensitivity in the near future. *Moody et al.* (2003) are devel-

oping an instrument for use in an aircraft or ship with an accuracy of $< 1 \text{ EHz}^{-1/2}$. Superconducting Gravity Gradiometer (SGG) designs for space-borne missions, which require $10^{-4} \text{ EHz}^{-1/2}$ sensitivity, have been demonstrated to achieve $0.02 \text{ EHz}^{-1/2}$ in the lab. Enhancements to the SGG, e.g., by employing magnetically suspended test masses (versus the current mechanical suspension), may provide improved sensitivity by several orders of magnitude yielding resolutions of $10^{-5} \text{ EHz}^{-1/2}$ (*Moody et al.*, 2002).

We suggest that highly sensitive SGGs designed for terrestrial observations may allow for the direct measurement of post-seismic gravity gradients arising from large events such as the Joshua Tree-Landers-Hector Mine sequence. Plans to incorporate the underlying regional stress, as well as more complex fault geometries, are under way presently. Moreover, extension of the method to include thrusting fault solutions, which contain larger gravity signals than strike-slip faults, may produce more readily observed signals.

REFERENCES

- Bell, R. E., Gravity gradiometry resurfaces, *The Leading Edge*, January, 55-59, 1997.
- Bennett, R. A., R. E. Reilinger, W. Rodi, Y. Li, M. N. Toksöz, and K. Hudnut, Coseismic fault slip associated with the 1992 $m_w 6.1$ Joshua Tree, California, earthquake: Implications for the Joshua Tree-Landers earthquake sequence, *J. Geophys. Res.*, 100(B4), 6443-6461, 1995.
- Bowman, D. D., and G. C. P. King, Accelerating seismicity and stress accumulation before large earthquakes, *Geophys. Res. Lett.*, 28, 4039-4042, 2001.

- Chinnery, M. A., The deformation of the ground around surface faults, *Bull. Seis. Soc. Amer.*, 51(3), 355–372, 1961.
- Chinnery, M. A., The stress changes that accompany strike-slip faulting, *Bull. Seis. Soc. Amer.*, 53(5), 921–932, 1963.
- Freed, A. M., and J. Lin, Delayed triggering of the 1999 Hector Mine earthquake by viscoelastic stress transfer, *Nature*, 411, 180–183, doi: 10.1038/35075548, 2001.
- Hayes, T. J., K. F. Tiampo, J. B. Rundle, and J. Fernández, Gravity changes from a stress evolution earthquake simulation of California, *J. Geophys. Res.*, 111, B09,408, doi:10.1029/2005JB004092, 2006.
- King, G. C. P., R. S. Stein, and J. Lin, Static stress changes and the triggering of earthquakes, *Bull. Seis. Soc. Amer.*, 84(3), 935–953, 1994.
- Lin, J., and R. S. Stein, Stress triggering in thrust and subduction earthquakes, and stress interaction between the southern San Andreas and nearby thrust and strike-slip faults, *J. Geophys. Res.*, 109, B02,303, doi:10.1029/2003JB002607, 2004.
- Mansinha, L., and D. E. Smylie, The displacement fields of inclined faults, *Bull. Seis. Soc. Am.*, 61(5), 1433–1440, 1971.
- Moody, M., H. J. Paik, and E. R. Canavan, Three-axis superconducting gravity gradiometer for sensitive gravity experiments, *Rev. Sci. Instrum.*, 73, 3957, 2002.
- Moody, M., H. J. Paik, and E. R. Canavan, Three-axis superconducting gravity gradiometer for sensitive gravity experiments, *Rev. Sci. Instrum.*, 74, 1310, 2003.

- Okada, Y., Surface deformation due to shear and tensile faults in a half-space, *Bull. Seis. Soc. Amer.*, 75(4), 1135–1154, 1985.
- Okada, Y., Internal deformation due to shear and tensile faults in a half-space, *Bull. Seis. Soc. Amer.*, 82(2), 1018–1040, 1992.
- Okubo, S., Potential and gravity changes raised by point dislocations, *Geophys. J. Int.*, 105, 573–586, 1991.
- Okubo, S., Gravity and potential changes due to shear and tensile faults in a half space, *J. Geophys. Res.*, 97(B5), 7137–7144, 1992.
- Rundle, J. B., Gravity changes and the Palmdale uplift, *Geophys. Res. Lett.*, 5(1), 41–44, 1978.
- Saad, A. H., Understanding gravity gradients—a tutorial, *The Leading Edge*, August, 942–949, 2006.
- Samsonov, S., and K. Tiampo, Analytical optimization of a DInSAR and GPS dataset for derivation of three-dimensional surface motion, *IEEE Geoscience and Remote Sensing Letters*, 3(1), 107–111, 2006.
- Stein, R. S., G. C. P. King, and J. Lin, Stress triggering of the 1994 $m = 6.7$ Northridge, California, earthquake by its predecessors, *Science*, 265, 1432–1435, 1994.
- Tiampo, K. F., J. B. Rundle, S. A. McGinnis, and W. Klein, Pattern dynamics and forecast methods in seismically active regions, *Pure Appl. Geophys.*, 159(10), 2429–2467, 2002.
- Toda, S., R. S. Stein, K. Richards-Dinger, and S. Bozkurt, Forecasting the evolution of seismicity in southern California: Animations built on earthquake stress transfer, *J. Geophys. Res.*, 110, B05S16, doi: 10.1029/2004JB003415, 2005.

Walsh, J. B., and J. R. Rice, Local gravity changes resulting from deformation, *J. Geophys. Res.*, 84(B1), 165-170, 1979.

CONCLUSIONS

This is the end

Beautiful friend

Jim Morrison

THESIS FINDINGS



N THIS thesis the application of gravity as a tool for seismic hazard mitigation was investigated. By developing the gravity evolution of the system via VC, we were able to investigate long-term trends that would otherwise not be possible. Solutions of the change in gravity due to long-term tectonic plate loading and co-seismic events were found and applied using historical earthquakes and a stress-evolution fault model. Moreover, interpretation of the resultant gravity signals has allowed us to understand fundamental physical relationships between faults and their orientation with respect to each other and the long-term loading plate forces. Further more, for the first time, solutions of the gravity gradients for a vertical, strike-slip fault within an elastic half-space were developed and used to examine the Joshua Tree earthquake of 1992. The resultant gravity gradient map, whose physical interpretation allows us to define the edges of the deformation field following a seismic event, exhibits compelling correlation with Coulomb stress change plots. This is significant in that it may allow researchers to physically map out the changes arising from stress and strain at depth.

In summary, it was found that:

- (i) The gravity signal of the long-term tectonic plate loading is observable by permanent gravimeters and, in the future, likely observable by portable instruments.
- (ii) Dilatational gravity signals from unstable, seismic slip are within the range of portable instruments for strike-slip systems.
- (iii) Fault geometry controls the spatial distribution of the gravity signal, differing greatly in its spatial distribution than traditional single plane solutions.
- (iv) Fault orientation with respect to the plate velocity plays a key role in determining the type of precursory dilatational gravity signal observed.
- (v) Spatial distribution comparisons of the gravity gradients and Coulomb stress changes suggest that the subsurface stress changes can be approximated by the dilatational gravity gradients, and thus measured using gravity as a proxy.

IMPLICATIONS

Results from this thesis suggest that the creation of a gravity monitoring network of strategically located permanent gravimeters (e.g, absolute gravimeters and superconducting gravimeters) is warranted. Coupled with periodic field campaigns, gravity data collection may offer researchers further constraints on the current state of subsurface stress and strain. Furthermore, the use of gravity gradients as a proxy for the spatial distribution of the subsurface deformation field may allow researchers to directly measure the extent of Coulomb stress

changes, which are inherently unobservable, and can only be calculated and interpreted. By incorporating the gravity data into these solutions, a more accurate estimate of the subsurface stress and strain may be obtained. Such information can be used to further understand the physical processes operating at depth, as well as assist studies for seismic hazard mitigation.

FUTURE WORK

Future studies into various aspects of this research include:

- (i) The development of finite element models to further quantify the relationship between gravity and the shear and normal components of stress.
- (ii) Incorporation of viscoelastic effects into the gravity solutions for purposes of examining more accurately how the gravity signal develops over time. Currently, the time component is a static value, and estimates of the free-air component become unrealistic for long time intervals.
- (iii) Determining the general solution for the gravity gradients, for faults with arbitrary orientation, dip, and slip-mechanisms, including their application into a complex network composed of many fault segments.
- (iv) The development of more accurate gradiometers, designed for permanent, terrestrial observations. Currently, not much work is done in this area as the main source of funding is for mineral exploration (which requires less resolutions than seismic hazard applications) or space-borne missions. By adapting the space-borne instruments to use a magnetically suspended sphere, as

opposed to the current mechanically suspended mass, the resolution for gradient observations is possible. Indeed, it is the use of a magnetically suspended sphere which allows the superconducting gravimeter to achieve its nGal resolution.

APPENDIX A

CODE LISTINGS

There is much Obi-wan did not tell you.

Darth Vader

The Compact Disc provided contains all of the codes from Chapter 1 as a compressed `tar.gz` file. The codes are unpacked by issuing the command:

```
$ tar -zxvf GRAV90_CODES_Oct_2007.tar.gz
```

This will create several directories under the main directory, entitled `PUBLIC_CODES`. Contained within are several `README` files which describe the use of the codes beyond the description provided in Chapter 1. The programs have been tested with Linux (Kubuntu and Fedora Core) and require a `FORTRAN90` compiler, a `FORTRAN77` compiler (for the history programs only), a working distribution of `LATEX`, and `IDL 6.1` or greater (for the visualization routines).

APPENDIX B

COPYRIGHT PERMISSIONS

It could be said of me that in this book I have only made up a bunch of other men's flowers, providing of my own only the string that ties them together.

Michel de Montaigne

B.I COAT OF ARMS

Permission for The University of Western Ontario Coat of Arms to appear on the title page of this thesis was granted by Terry Rice, Director, Creative Services, Communications and Public Affairs, The University of Western Ontario. All questions regarding its use on the title page should be directed to him (tjrice@uwo.ca).

B.2 JOURNAL OF GEOPHYSICAL RESEARCH



1 November 2007

Tyler Joseph Hayes
The University of Western Ontario
Geophysics with Scientific Computing
Department of Earth Sciences
B&GS Room 154
London, Ontario N6A 5B7
Canada

Dear Mr. Hayes:

We are pleased to grant permission for the use of the material requested for inclusion in your thesis. The following non-exclusive rights are granted to AGU authors:

- All proprietary rights other than copyright (such as patent rights).
- The right to present the material orally.
- The right to reproduce figures, tables, and extracts, appropriately cited.
- The right to make hard paper copies of all or part of the paper for classroom use.
- The right to deny subsequent commercial use of the paper.

Further reproduction or distribution is not permitted beyond that stipulated. The copyright credit line should appear on the first page of the article or book chapter. The following must also be included, "Reproduced by permission of American Geophysical Union." To ensure that credit is given to the original source(s) and that authors receive full credit through appropriate citation to their papers, we recommend that the full bibliographic reference be cited in the reference list. The standard credit line for journal articles is: "Author(s), title of work, publication title, volume number, issue number, page number(s), year. Copyright [year] American Geophysical Union."

If an article was placed in the public domain, in which case the words "Not subject to U.S. copyright" appear on the bottom of the first page or screen of the article, please substitute "published" for the word "copyright" in the credit line mentioned above.

Copyright information is provided on the inside cover of our journals. For permission for any other use, please contact the AGU Publications Office at AGU, 2000 Florida Ave., N.W., Washington, DC 20009.

Sincerely,

A handwritten signature in black ink, appearing to read "Michael Connolly".

Michael Connolly
Journals Publications Specialist

A worldwide scientific community that advances, through unselfish cooperation in research, the understanding of Earth and space for the benefit of humanity.
2000 Florida Avenue, NW, Washington, DC 20009-1277 USA Tel: +1 202.462.6900 Fax: +1 202.328.0566 www.agu.org

FIGURE B.1: Facsimile of the copyright release for Chapter 2.

CIRICULUM VITA

Tyler Joseph Hayes

BORN: April 8th, 1975

POST SECONDARY EDUCATION

The University of Western Ontario

London, Canada

1999-2001 M.Sc.

The University of Western Ontario

London, Canada

1994-1999 B.Sc.

HONOURS AND AWARDS

SEG Lucien LaCoste Scholarship
Ontario Graduate Scholarship, Worth
UWO Geophysics Travel Scholarship
The Presidents Scholarship
Special University Scholarship

2006

2006,2005,2004

2004,2003

2003

2000,2001

RELATED WORK EXPERIENCE

Lecturer

The University of Western Ontario

ES 320a, Exploration methods

Fall 2005

Teaching Assistant

The University of Western Ontario

1999-2001, 2003-2005

PUBLICATIONS

- Hayes, T., and L. Mansinha, Changes in the inertia tensor and gravitational waves, in *Canadian Geophysical Union Spring Meeting*, CGU, (ORAL PRESENTATION), 2001.
- Hayes, T., K. Tiampo, and J. Rundle, Co-seismic gravity modeling of a fault network, *Eos. Trans., AGU Fall Meeting Suppl.*, 85(47), G11A-0763, (ABSTRACT), 2004a.
- Hayes, T., K. Tiampo, and J. Rundle, Long period co-seismic gravity modelling of silent slip earthquakes along the Cascadia subduction zone, *Eos. Trans., AGU Joint Assembly Suppl.*, 85(17), G21A-04, (ABSTRACT), 2004b.
- Hayes, T., S. Valluri, and L. Mansinha, Gravitational effects from earthquakes, *Canadian Journal of Physics*, 82(12), 1027-1040, 2004c.
- Hayes, T., K. Tiampo, and J. Rundle, Application of a gravity Green's function method using a stress-evolution earthquake simulation California, *Eos. Trans., AGU Fall Meeting Suppl.*, 86(52), G33A-0024, (ABSTRACT), 2005a.
- Hayes, T., K. Tiampo, and J. Rundle, Gravity changes over California using a time-dependent earthquake model, *SCEC Annual Meeting, XV*, (ABSTRACT), 2005b.
- Hayes, T., K. Tiampo, and J. Rundle, Using gravity as a proxy for strain accumulation in complex fault networks, *Eos. Trans., AGU Fall Meeting*, 87(52), G43B-0998, (ABSTRACT), 2006a.
- Hayes, T., K. Tiampo, and J. Rundle, A gravity evolution examination of the Landers-Hector Mine sequence, *SCEC Annual Meeting, XVI*, (ABSTRACT), 2006b.

Hayes, T. J., Possible gravitational waves from earthquakes: Estimates for the far field and implications for near field experiments, Masters thesis, The University of Western Ontario, 2001.

Hayes, T. J., K. F. Tiampo, J. B. Rundle, and J. Fernández, Gravity changes from a stress evolution earthquake simulation of California, *J. Geophys. Res.*, 111, B09,408, doi:10.1029/2005JB004092, 2006c.

Mansinha, L., and T. Hayes, A search for gravitational disturbances from earthquakes, *J. Geodetic Soc. Jap.*, 47(1), 359–363, 2001.

Tiampo, K. F., J. Fernández, T. Hayes, and G. Jentzsch, Modeling of stress changes at Mayon volcano, Philippines, *Pure appl. geophys.*, 164, 819–835, doi:10.1007/s00024-007-0189-4, 2007.